Renewable Energy 184 (2022) 677–699

Contents lists available at ScienceDirect

Renewable Energy

journal homepage: www.elsevier.com/locate/renene

Numerical modelling and dynamic response analysis of a 10 MW semi-submersible floating offshore wind turbine subjected to ship collision loads

Zhaolong Yu [a, b, *], Jørgen Amdahl [a, b], Martin Rypestøl [a, b], Zhengshun Cheng [c]

[a] Department of Marine Technology, Norwegian University of Science and Technology (NTNU), Norway
[b] Center for Autonomous Marine Operations and Systems (AMOS), Norwegian University of Science and Technology (NTNU), Norway
[c] Department of Naval Architecture, Civil and Ocean Engineering, Shanghai Jiao Tong University, China

ARTICLE INFO

Article history:
Received 15 December 2020
Received in revised form
29 November 2021
Accepted 1 December 2021
Available online 5 December 2021

Keywords:
Ship collision
Floating offshore wind turbine
OO-STAR floater
Energy absorption
Global response

ABSTRACT

The number of installed offshore wind turbines is continuously growing worldwide in recent years. Offshore wind farms are generally located near the coast close to traffic lanes and are exposed to the risk of collisions from visiting and passing ships. Potential consequences of collisions may vary from local structural damage to the detachment of turbine nacelles and rotors, and even tower collapse and capsizing of the turbine platform, causing significant economic loss and fatalities.

This paper investigates ship collision responses of a semi-submersible floating offshore wind turbine (FOWT), i.e. the OO-STAR floater with the DTU 10 MW blades, using the nonlinear finite element code USFOS. The OO-STAR floater is made of post-tensioned concrete designed by Dr. techn. Olav Olsen. The striking ships are selected to be a modern supply vessel of 7500 tons and a shuttle tanker of 150,000 tons, representing respectively service/coastal merchant vessels and large passing vessels. Modelling of the FOWT in USFOS is described in detail including the OO-STAR floater, the DTU 10 MW turbine blade, the turbine tower, and the mooring system. The modelled hydrodynamic loads include buoyancy loads and motion induced radiation loads using the Morrison equation. The effects of external waves and currents are assumed to be small and ignored in all directions. Eigenmode analysis of the turbine model is performed to verify the established model.

Global collision response analyses of the FOWT were performed in both parked and operating conditions. The ship resistance is modelled as nonlinear springs in USFOS containing force displacement curves simulated in LS-DYNA. In operating conditions, wind loads are introduced including wind thrust loads and wind induced torque to rotate the turbine blades. The changes of upstream wind speeds and rotor/wake interactions during collisions are neglected. The results are discussed with respect to energy absorption of the ship and the FOWT, and structural responses of the FOWT including global motions, nacelle accelerations, tower clearance, tower vibrations, and responses of the mooring system.

1. Introduction

Offshore wind energy is one of the most promising renewable energy resources in the coming decades. Compared to onshore turbines, offshore turbines provide higher wind speeds for electricity generation and less noises. In recent years, the number of offshore wind farms is growing rapidly. By the end of 2019, Europe has a total of 22.1 GW of offshore winds installed, of which 3.62 GW is installed in 2019 [1]. The majority of installed offshore wind farms are bottom fixed turbines with monopile or jacket foundations in shallow water, i.e.<50 m. For areas with a water depth larger than 50 m, bottom fixed offshore turbines are not economically attractive and floating offshore wind turbines (FOWTs) are preferred. Floating offshore wind turbines consist of a floater, which is connected to the seabed by mooring lines. The most common floating foundations are the semi-submersible type, spar type, tension leg type and barge type floaters, refer to Fig. 1 [2].

Offshore wind farms are generally located near the coast close to traffic lanes. From the safety point of view, the probability of

* Corresponding author. Department of Marine Technology, Norwegian University of Science and Technology (NTNU), Norway.
E-mail address: zhaolong.yu@ntnu.no (Z. Yu).

https://doi.org/10.1016/j.renene.2021.12.002

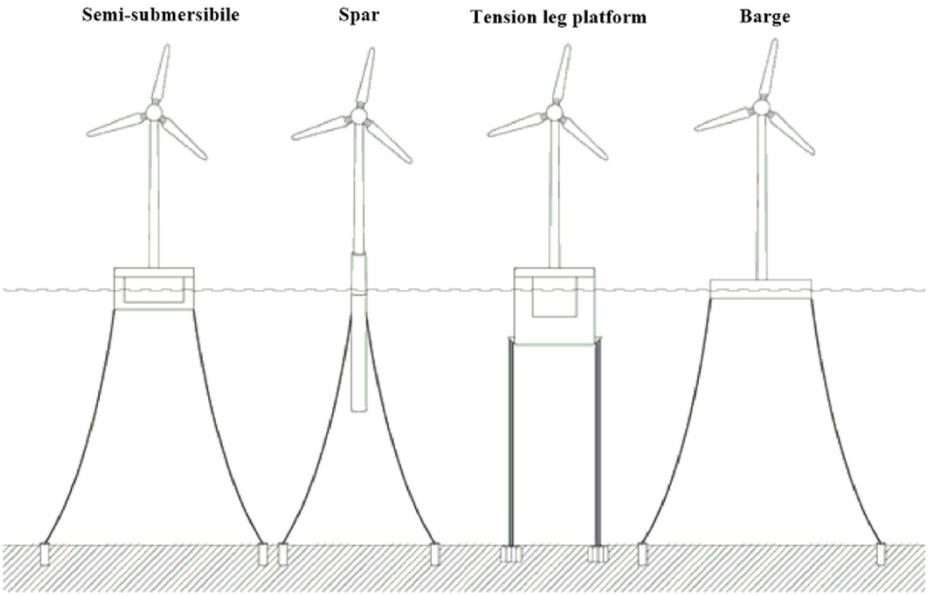

Fig. 1. Four common floater types for floating offshore wind turbines, DNVGL-ST0119 [2].

collisions from a merchant ship during an avoidance maneuver of another vessel or free drift following a propulsion damage cannot be neglected. In addition, offshore supply vessels operating close to the wind farms may also hit the turbine accidently. It is crucial to assess the dynamic response of offshore wind turbines subjected to collisions from passing and visiting ships and to design structures against such accidental actions.

For ship collisions with bottom fixed offshore wind turbines, Biehl and Lehmann [3] studied the behavior of three foundation structures i.e. monopile, tripod, and jacket type offshore wind turbines subjected to ship collisions. LS-DYNA was used to simulate the damage caused by collisions of four different ship types: single (200,000 tons) and double (45,000 tons) hull tankers, bulk carriers (25,000 tons), and container ships (52,000 tons). The ship caused large deformations of the turbine foundations, which may be completely torn off in extreme cases. The nacelle and the rotor may fall on the deck of the striking vessel. The collision loads caused local damage on the ship hull with possible oil leakage. Bela et al. [4] investigated the response of offshore wind turbine monopile foundations collided by a rigid ship bow, and found that the turbine exhibited a quasi-elastic response associated with minor plastic deformations in small energy collisions, and elastoplastic response associated with large plastic deformations at the impact point and near the mudline, and even collapse of the entire turbine structure in large energy impacts. Pedersen [5] presented an analytical model for the external dynamic calculation of ship collisions against bottom supported wind turbines. Numerical results showed that for piled towers, the structural flexibility plays an important role to reduce structural damage. Kroondijk [6] studied a 190,000-ton tanker colliding with a jacket foundation based offshore turbine using USFOS. Le Sourne et al. [7] and Pire et al. [8] investigated jacket foundations of offshore wind turbines subjected to ship collisions and proposed simplified analytical solutions for the collision resistance. Song et al. [9] studied impacts between a 4600-ton vessel and a 5-MW monopile offshore wind turbine. The effects of aerodynamic damping, ship impact velocity, mean wind speed, wind direction, and ship bow stiffness on the collision responses were analyzed.

For ship collision with floating offshore wind turbines, Echeverry et al. [10] simulated a spar type FOWT subjected to collisions from a supply vessel of 5000 tons using LS-DYNA. The vessel motions and hydrodynamic effects are included with MCOL. The numerical results showed significant damage of the turbine tower cross sections. No experiments or scaled tests were found from the literature related to impact of scaled floating offshore wind turbines. The challenges for conducting such tests are the large expenses in the first place and the coupled nature of the problem involving hydrodynamics, structural mechanics, and aerodynamics, which makes scaling of the model difficult.

The literature study shows that research on ship collisions with floating offshore wind turbines is quite limited and knowledge on the associated risk and consequences is not well established. This paper investigates the dynamic response of a 10 MW semi-submersible FOWT subjected to ship collision loads. The selected turbine adopts the design from the LIFES50+ project [11], which consists of the OO-STAR semi-submersible floater designed by Dr. techn. Olav Olsen AS [12] (see Fig. 2), the DTU 10 MW Reference Wind Turbine (RWT) [13], and the detailed designs of turbine tower and mooring lines. The striking vessels are selected to be a modern supply vessel of 7500 tons and a characteristic shuttle tanker of 150,000 tons, representing respectively service/coastal merchant

Fig. 2. The OO-STAR floating offshore wind turbine design by Dr. techn. Olav Olsen AS [12].

vessels and large passing vessels. The ship-FOWT collision analysis is carried out by using the nonlinear finite element software USFOS [14]. USFOS is a time domain program for ultimate strength and progressive collapse analysis of framed offshore structures, and has been used extensively in the analysis of framed structures under environmental and accidental loads, such as jackets and jack-ups [15], floating bridges [16] and fish farms [17]. Modelling of the floating wind turbine platform in USFOS is described, and the established model is verified by eigenmode analysis and comparing the relevant values in the LIFES50+ and DTU reports. The results of ship-FOWT collisions are discussed with respect to energy absorption of the ship and the FOWT, and structural responses of the FOWT including the global motions, the nacelle acceleration, the tower clearance, the tower vibrations, and the forces in the mooring system.

2. Description of the OO-STAR semi-submersible floating wind turbine concept and its modelling in USFOS

2.1. Modelling of the DTU 10 MW reference wind turbine

2.1.1. The turbine blade and tower

The DTU 10-MW reference rotor [13] is designed as a result of the Light Rotor project by DTU Wind Energy and Vestas. The main objective is to optimize the design of turbine blades to increase the stiffness and overall performance of the rotor, and at the same time the blade weight should be minimized. Some of the key parameters are summarized in Table 1.

The turbine blades are modelled based on a detailed geometric description provided in an openly accessible excel sheet. The blade is considered as composed of a number of discrete general beam elements, each with specific cross-section, structural properties, and mass. A total of 26 elements is created for each blade. Along the blade, the angle of attack varies due to the twisted blade segments.

The tower in the DTU report [18] is originally given for a land based turbine, but is extended in the LIFES50+ project [11] for floating offshore turbines. The latter is adopted in this study. The tower is cylindrical with linearly varying outer diameter from D = 11.385 m at the bottom (11 m above the mean surface level (MSL)) to D = 5.2 m at the top (115.63 m above MSL). The tower is subdivided into 27 sections, where the wall thickness is constant in each beam section and varies from 75 mm at the bottom to 29 mm at the top. Steel with a yield stress of 355 MPa is used for the tower. The total weight of the tower is 1.257e+3 tons. Tubular elements with high yield stress are used to connect the blades to the rotor and the rotor to the tower. The high yield strength is used to prevent any plasticity in the connection members. The hub and the nacelle are not explicitly modelled but are included as nodal masses at the blade connection and the top of the tower, respectively. The upper part of the turbine with the assembly of the blades and tower is shown in Fig. 3.

Table 1
Key parameters of the DTU 10 MW reference wind turbine.

Parameter	DTU 10 MW RWT
Number of blades	3
Rotor diameter	178.3 m
Hub diameter	5.6 m
Hub Overhang	7.1 m
Rotor mass	227,962 kg
Nacelle mass	446,036 kg
Shaft Tilt Angle	5 deg
Rotor Pre-cone Angle	−2.5 deg
Maximum Rotor Speed	9.6 rpm
Rated Wind Speed	11.4 m/s

2.1.2. Tower clearance

Sufficient tower clearance is crucial to prevent the blades from hitting the turbine tower. This is especially important to check in accidental ship collision conditions. Modern wind turbines have a tilted shaft, a cone angle, and prebend of the blades that all increases the distance between the blade tips and tower, refer to Fig. 4. The tower clearance for the 10 MW DTU RWT with the land-based tower is 18.26 m [18] when loading of the blades are not accounted for. With the increased diameter in the floating turbine tower, the tower clearance is estimated to be reduced to 16.5 m.

According to the DTU report, the 10 MW RWT has a tilted shaft with length 7.1 m positioned at 2.75 m above the top of the tower. In the USFOS model, prebend of the blades and the tilt are included, see Fig. 3. The additional 2.75 m height is neglected with minor influence. The cone angles of the blades are not modelled. The resulting tower clearance in the USFOS model is estimated to be 12.8 m without wind loads. This is conservative with respect to the risk of blades hitting the tower.

2.1.3. Model verification

The models of the turbine blades and tower in USFOS are verified by conducting eigenvalue analysis and comparing with the corresponding values in the reports. The eigenvalue analysis is carried out for an isolated blade, the tower with a rigid rotor and the combined tower and rotor with realistic materials, respectively.

2.1.3.1. • *Eigenmode analysis of an isolated blade.* Table 2 compares natural frequencies for an isolated blade from the DTU report [18] and the USFOS analysis. The first two flap and edge modes are crucial and analyzed. The deviation is relatively small, especially for the 1st modes. This demonstrates that modelling of the turbine blade is reasonably correct.

2.1.3.2. • *Eigenmode analysis of the tower with the rigid rotor.* Table 3 compares the natural frequencies for the turbine tower with a rigid rotor from the LIFES50+ D4.2 report [11] and USFOS analysis. Natural frequencies for the first two fore-aft modes and side-side modes are considered. The USFOS analysis shows good agreement of the obtained natural frequencies for different modes. This indicates sound modelling of the tower flexibilities and reasonable overall mass distributions of the rotor, hub and the nacelle. The corresponding eigenmodes of the tower are displayed in Fig. 5.

2.1.3.3. • *Eigenmode analysis of the assembled tower and rotor.* The turbine blades and tower are verified separately in the above

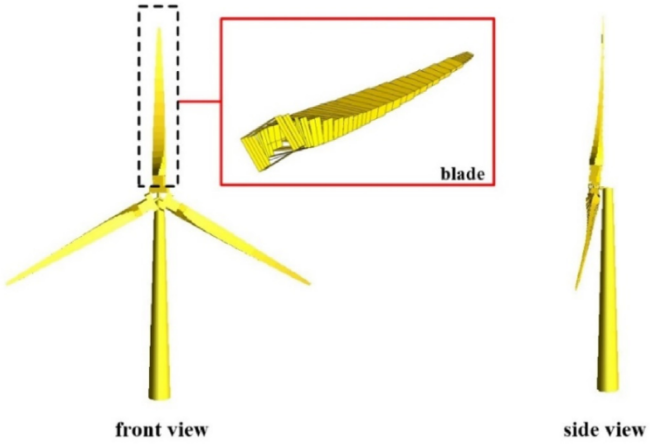

Fig. 3. The USFOS model for the turbine blades and tower.

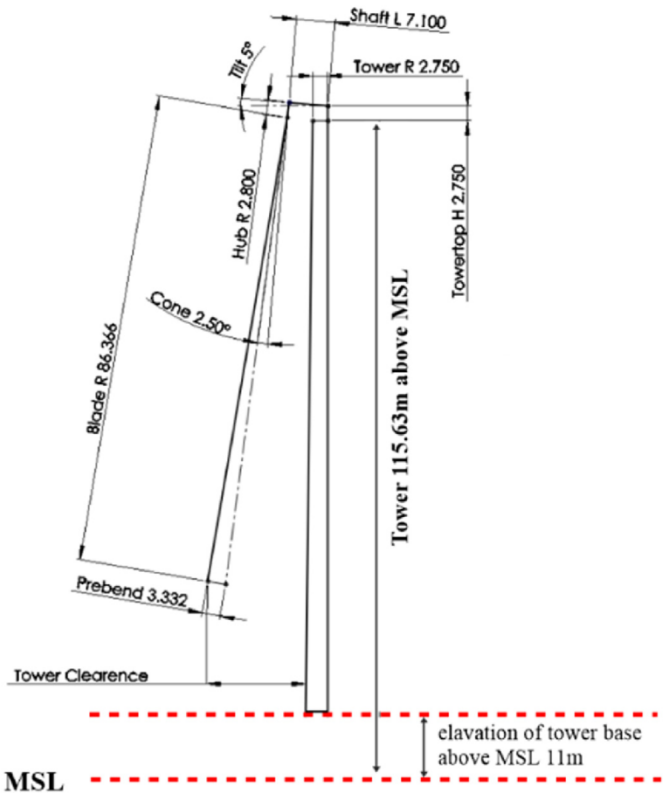

Fig. 4. Description of the tower clearance.

eigenmode analysis. When the blades and tower are assembled, they interact. Table 4 shows natural frequencies for the first 5 modes of the assembled turbine tower and rotor with USFOS analysis. No direct data is available for comparison from the LIFES50+ report with the floating-based turbine tower. Natural frequencies for the assembled tower and rotor system are considered reasonable in view of the good agreement when the tower and blades act alone. From Table 4, the first two modes are dominated by the tower, while the latter three are governed by the rotor. The first 5 eigenmodes are plotted in Fig. 6. The frequencies obtained are also very logical with respect to those of the isolated sub-models.

2.2. Modelling of the OO-STAR floater and the mooring system

2.2.1. The OO-STAR floater

The OO-Star Wind Floater was designed by Dr. techn. Olav Olsen AS [12] in response to the need for innovative solutions for offshore floating winds. The floater is capable of supporting heavy turbines under harsh environmental conditions and can be positioned in areas that are unsuited for bottom-fixed turbines. It is scalable for wind turbine generators of well over 12–15 MW without size limitations related to assembly and installation.

The floater consists of a central column and three outer columns mounted on a star-shaped pontoon with a bottom slab. All the columns have a cylindrical upper part and a tapered lower part. The main material is post-tensioned concrete, which yields a higher displaced volume as for steel structures. The geometrical properties of the floater are marked in Fig. 7. The distance between the central column and the outer column is 37 m. The horizontal pontoon

Table 2
Comparison of natural frequencies for an isolated blade.

Mode	Natural frequency [Hz] from DTU report	Natural frequency [Hz] of the USFOS model	Deviation [%]
1st flap mode	0.61	0.61	0
1st edge mode	0.93	0.91	−2.1
2nd flap mode	1.74	1.82	4.6
2nd edge mode	2.76	2.91	5.4

Table 3
Comparison of natural frequencies for the turbine tower with a rigid rotor.

Mode	Natural frequency [Hz] from DTU report	Natural frequency [Hz] of the USFOS model	Deviation [%]
1st fore-aft mode	0.553	0.571	3.2
1st side-side mode	0.544	0.559	2.7
2nd fore-aft mode	2.437	2.468	1.3
2nd side-side mode	2.107	2.022	−4.0

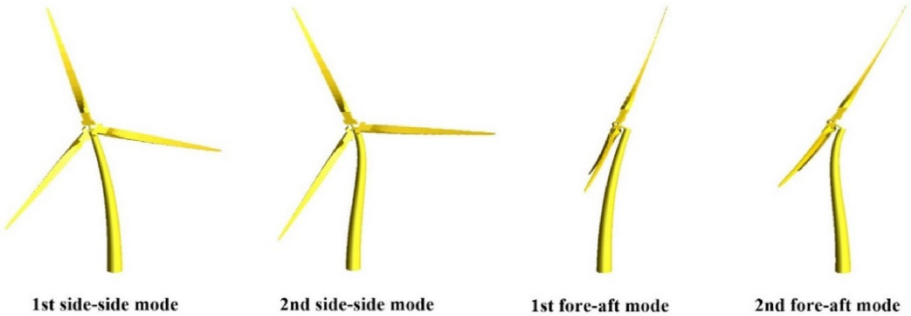

Fig. 5. Eigenmodes of the turbine tower with a rigid rotor.

Table 4
Natural frequencies for the assembled turbine tower and rotor.

Mode	Natural frequency [Hz] of the USFOS model with the *floating-based* tower
1st tower fore-aft mode	0.512
1st tower side-side mode	0.533
1st asymmetric flap with yaw	0.570
1st asymmetric flap with tilt	0.595
1st collective flap mode	0.680

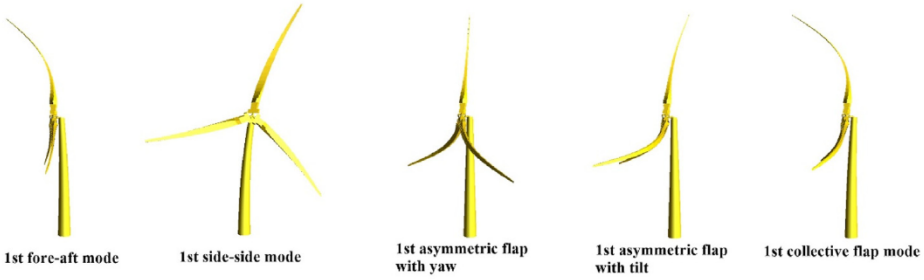

Fig. 6. Eigenmodes of the assembled turbine tower and rotor.

elements connecting the columns have a width of 16 m and a height of 7 m. The slab attached underneath the pontoons has a width of 17 m, adding 0.5 m at each side. The central column has a diameter of 12.05 m at the tower base interface. It has a tapered shape below with a diameter which increases linearly over a length of 17.3 m−16.2 m at the pontoon interface. The outer columns have a diameter of 13.4 m at the top, and a conical section below, which has a length of 11 m with a diameter of 15.8 m at the pontoon interface [11]. The coordinate system on the floater is defined in Fig. 7 with the origin located on the mean surface plane.

The OO-Star Wind Floater is modelled by beam elements in USFOS. The floating structure is subdivided into different sections. The material density for each section is adjusted so as to obtain equilibrium of gravity and buoyancy forces at the correct draft of the floater with the tower, the rotor and the mooring system assembled. The tower bottom is 22 m above the bottom of the floater. The assembled model is shown in Fig. 8, and the mooring system is described in *Section 2.2.2*. Buoyancy is calculated by the displaced water volume based on submerged geometric surfaces in USFOS. Gravity and buoyancy are applied at the same time instant, and the nodal z displacement at the tower-floater intersection is evaluated as plotted in Fig. 8. The nodal z displacement oscillates within ±0.15 at an equilibrium of 0.0 when the floater gets stable, indicating correct draft of the floater. The properties of the obtained floater model including the mass, center of mass and moments of inertia are compared with those from the LIFES50+ D4.2 report [11] in Table 5. The differences are quite small, demonstrating a sound modelling of the floater.

2.2.2. The mooring system

The mooring system on the OO-Star Wind Floater is a catenary system with three mooring lines, where the horizontal angle between two chains is 120°. At each line there is a clumped mass of 50 tons attached. The layout is shown in Fig. 9 [11]. The main parameters of the mooring system are summarized in Table 6.

The mooring lines are modelled according to the coordinates given in the LIFES50+ D4.5 report [19]. Beam elements with circular cross-sections are used. The density of the mooring line material density is 7850 kg/m^3, while the diameter and thickness are adjusted to fit the exact mass distribution. The extensional stiffness is obtained by modifying elastic modulus based on the cross-sectional area. The established mooring system in equilibrium state is shown in Fig. 8. The upper part of the mooring line from the fairlead to the clamp mass is divided into 10 elements, while the lower part from the clamp mass to the anchor point are modelled with 30 elements. Because part of the lower mooring lines may lie on the seafloor when buoyancy and gravity forces reach an equilibrium, we model nonlinear contact springs between nodes of the lower part of the mooring line and the seabed. The contact spring stiffness is zero when the node is above the seabed and is large otherwise. This avoids penetration of the seabed by the mooring line. Nodal springs at the anchor points are established for modelling the soil and frictional stiffness. The anchor stiffness is adjusted to obtain the correct equilibrium position of the clamp mass. Fig. 10 (left) shows the time history of z displacement of the clamped mass when gravity and buoyancy forces are loaded. The clamp mass oscillates about its target equilibrium position in general. Fig. 10 (right) compares the pre-tension force at the fairlead and that from the report. Good agreement is obtained, indicating reasonable modelling.

2.2.3. Overall properties of the assembled wind turbine

The overall properties of the assembled wind turbine from USFOS are compared to those from the LIFES50+ D4.5 report [19] in Table 7. The total mass includes the ballasted platform, the tower and the rotor without the mooring lines. In USFOS, the natural periods of the assembled turbine are obtained by carrying out decay tests, where the hydrodynamic effects are described in *Section 3.1*. The overall mass and natural periods for the various turbine motions match well with those from the LIFES50+ report. This demonstrates reasonable reproduction of the FOWT with the combined OO-STAR floater and the DTU 10 MW reference turbine.

3. Modelling of environmental and ship collision loads

3.1. Hydrodynamic loads

The hydrodynamic loads considered in the collision analysis include buoyancy and motion induced radiation loads. No external waves or current loads are considered. Buoyancy and gravity loads are applied at the initial stage of analysis. The Morrison equation is often used to model hydrodynamic loads with two force

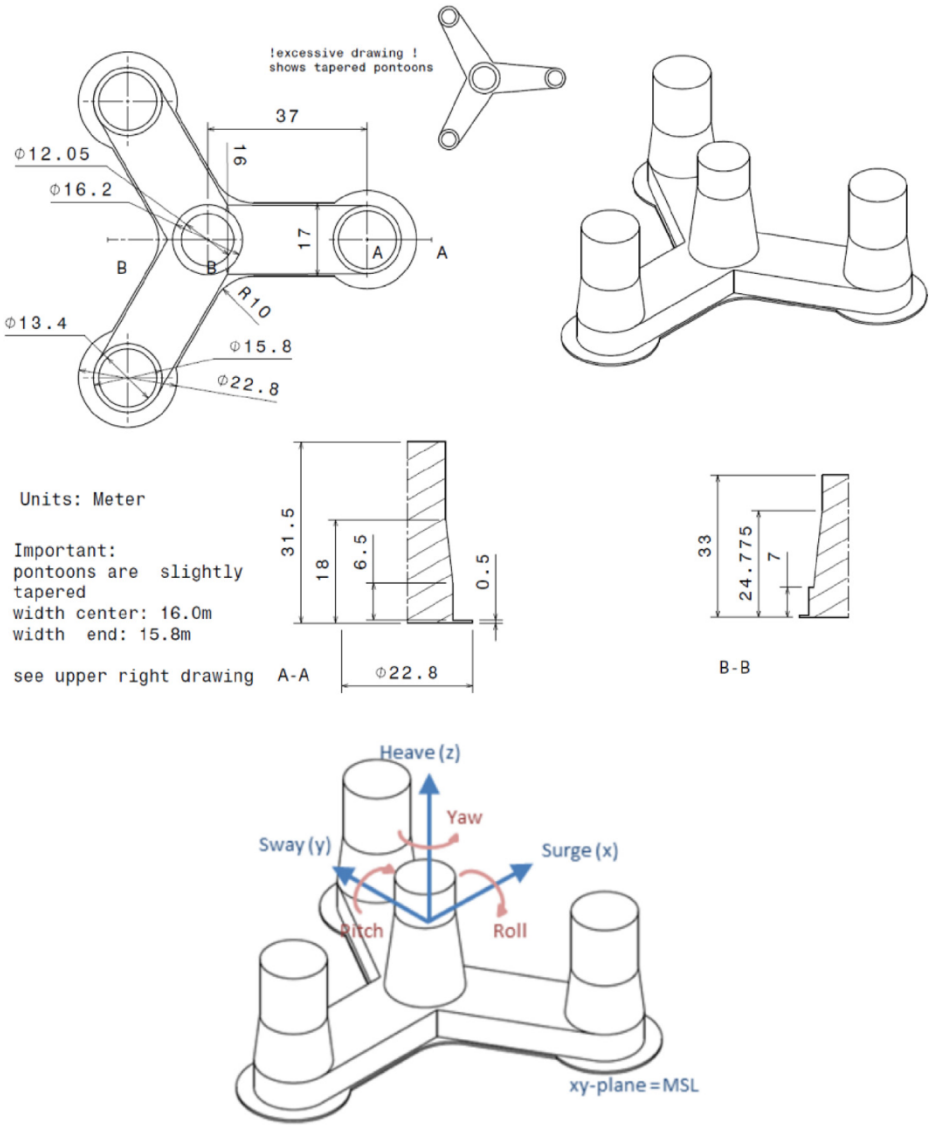

Fig. 7. Geometries and the coordinate system of the OO-STAR floater [11].

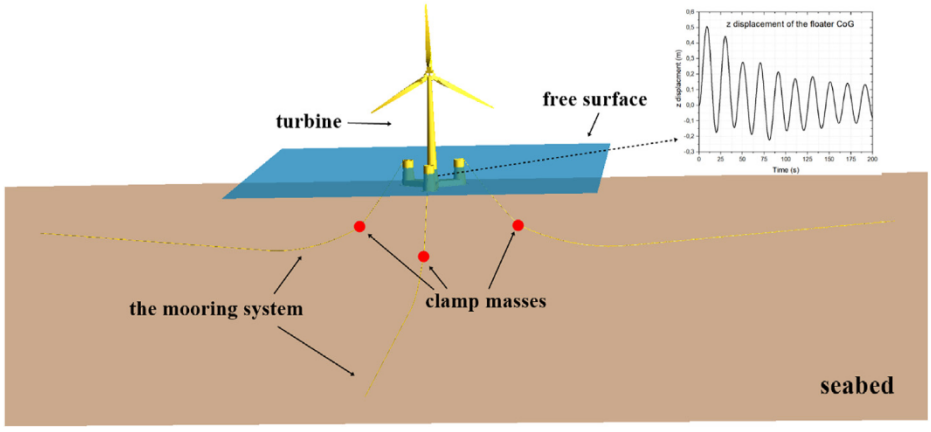

Fig. 8. The USFOS model for the turbine blades and tower.

Table 5
Comparison of properties of the OO-STAR floater.

Property	LIFES50+ report	The USFOS model	Deviation [%]
Overall substructure mass (excl tower, mooring), [kg]	2.171e+7	2.198e+7	1.2
Centre of Mass (CM) below MSL, [kg]	15.225	15.02	−1.3
floater roll inertia about CM, [kg m^2]	9.43e+9	9.29e+9	−1.4
floater pitch inertia about CM, [kg m^2]	9.43e+9	9.29e+9	−1.4
floater yaw inertia about CM, [kg m^2]	1.63e+10	1.57e+10	−3.7

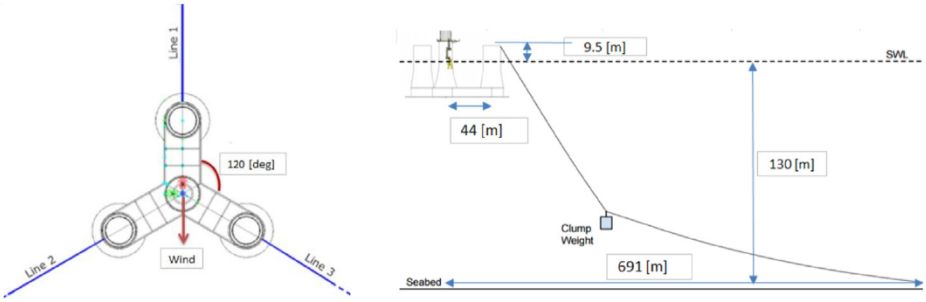

Fig. 9. Arrangement of the mooring line system for the OO-STAR floater, from [11].

Table 6
LIFES50+ OO-Star Wind Floater 10 MW mooring system properties.

Property	LIFES50+ report
Number of lines, [−]	3
Angle between adjacent mooring lines, [deg]	120
Total mass clump weight, [ton]	50
Location of fairleads above MSL, [m]	9.5
Pre-tension, [N]	1.67e+6
Extensional stiffness EA, [N]	1.506e+9
Effective hydraulic diameter of the chain, [m]	0.246
Physical chain diameter [m]	0.137
Hydrodynamic added mass coefficient, [−]	0.8
Hydrodynamic drag coefficient, [−]	2.0

components, i.e. an inertia force in phase with the local flow acceleration and a drag force proportional to the square of the instantaneous flow velocity. On a strip of length dz, the horizontal force can be expressed as,

$$dF = \rho C_m \frac{\pi D^2}{4} a_1 dz - \rho (C_m - 1) \frac{\pi D^2}{4} \ddot{\eta}_1 dz + \frac{1}{2} \rho C_d D dz (u - \dot{\eta}_1) \times |u - \dot{\eta}_1| \quad (1)$$

Where, ρ is the water density, η_1 is the horizontal motion of the strip, u and a_1 are horizontal undisturbed fluid velocity and acceleration evaluated at the strip center, C_m and C_d are the mass and drag coefficients, respectively.

The Morrison equation, however, has difficulties in modelling added masses in rotational motions, e.g. roll, pitch and yaw. In this study, the hydrodynamic inertia forces for the 6DOF motions of the floater are modelled as constant added masses at the turbine COG. Infinite frequency added masses from the LIFES50+ D4.5 report [19] are used, where the added masses at different frequencies were solved by the potential flow solver WAMIT [20]. For the drag forces acting on the floater, the Morrison equation is adopted by introducing C_d coefficients. C_m is set as 1, which gives no contribution according to Eq. (1). The C_d coefficient is taken from the LIFES50+ D4.5 report [19], being 0.7 for the floater columns, 2.05

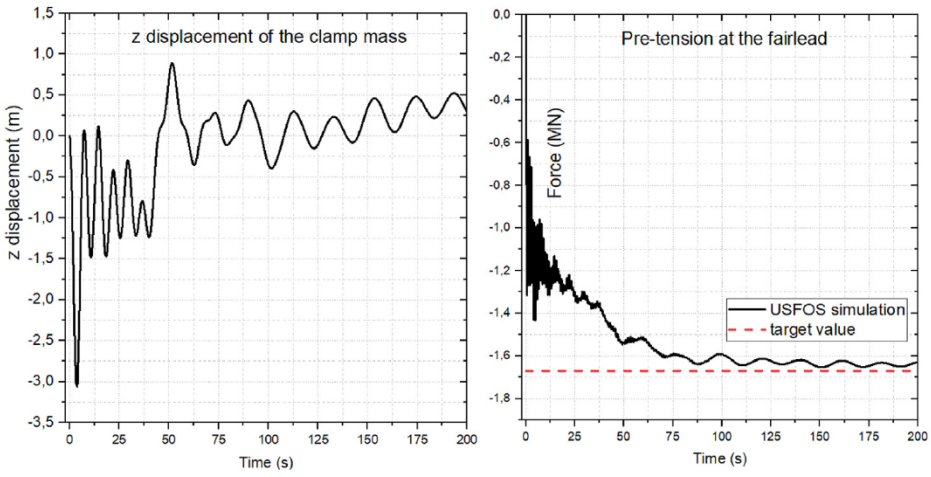

Fig. 10. (left) Nodal z displacement at the clamp mass when buoyancy and gravitational forces are loaded; (right) Pre-tension forces at the fairlead of the mooring lines.

Table 7
Comparison of total mass and natural periods of the assembled turbine model.

Property	LIFES50+ report	The USFOS model	Deviation [%]
Total mass (without the mooring lines), [kg]	2.361e+7	2.40e+7	1.7
Natural period surge, [s]	185.2	187.9	1.5
Natural period heave, [s]	20.92	20.00	−4.4
Natural period pitch, [s]	31.65	32.67	3.2
Natural period yaw, [s]	103.09	103.45	0.35

for the pontoons and 10 for the heave plates. For the mooring lines, the Morrison equation is used for both the inertia and drag forces with the mass and drag coefficients being 1.8 and 2.0 respectively according to the LIFES50+ D4.2 report [11].

3.2. Wind loads

The collision analyses shall include the 10 MW turbine in both parked and operating conditions. The ability to rotate the turbine blades is therefore essential in order to properly account for the inertia effects of rotating blades. The wind induced torque and associated control algorithm is not explicitly calculated in USFOS in this study. Instead, a zero-length spring is created at the blade connection. This spring has no stiffness in the torque degree of freedom while 'infinite' stiffness in the other five. An artificial torque moment is applied at the rotor, and the magnitude is adjusted until the maximum rotor speed of 9.6 rpm is achieved. After that, the torque moment is reduced to a small value to maintain the constant rotation speed.

Wind thrust forces normal to the rotor plane are crucial for calculating correctly the deflection of blades in operating conditions and subsequently tower clearances and bending moments. In this study, the DTU 10 MW reference wind turbine model was analyzed using the HAWC2 software [21]. The aerodynamic loads are calculated based on the blade element momentum (BEM) theory considering the effects of dynamic inflow, dynamic stall, hub and tip loss etc. The turbine blade is discretized into 50 sections. The thrust forces on each section are calculated, and then applied to the corresponding blade elements in USFOS as linearly varying line loads in each element. Because of the tilt, a small vertical force component of the wind thrust exists and is modelled in USFOS as well. Under steady wind condition with a rated wind speed of 11.4 m/s, the resultant thrust force is about 1546 kN, which agrees well with the results calculated by the BEM method from the DTU report [18]. The modelled thrust forces on turbine blades in USFOS are shown in Fig. 11.

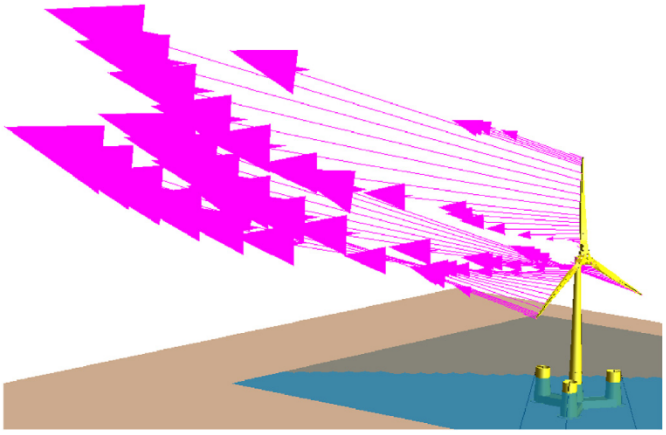

Fig. 11. Distribution of wind thrust loads on turbine blades.

3.3. Ship collision loads

3.3.1. Offshore supply vessel

For the design of offshore structures against collisions from service vessels, the NORSOK N003 standard [22] specifies that the selected vessel should not be less than 10,000 tons if no operational restrictions on allowable visiting vessel size are implemented. The corresponding speed shall be 3.0 m/s for head-on collisions and 2.0 m/s for sideways and stern impacts. DNVGL-RP-C204 [23] recommends load-deformation curves for standard 6500–10,000 tons vessels for collision analysis. In this study, the modern UT 745 platform supply vessel with a displacement of 7500 tons is selected. It has been used to verify the collision resistance of several North Sea oil & gas platforms. Although no specific requirements exist, it was chosen to use the same ship in this study as well to get information of the collision robustness of the OO-Star Floater. The ship may also be considered representative of impacts from moderate size merchant vessels. The principal dimensions of the vessel are given in Table 8. A hydrodynamic added mass of 40% for sideways and 10% for bow and stern impact are assumed.

For collision analysis with USFOS, a two-spring system is adopted, where the first spring represents ship stiffness and the second models contact. An example is displayed in Fig. 12 (left) for ship broadside collisions. For ship bow collisions, the ship stiffness includes two parts, one for the ship forecastle stiffness on the upper layer and the other for bulb stiffness on the lower layer as shown in Fig. 12 (right). The two ship springs are connected by rigid beams.

The ship mass including hydrodynamic added mass is modelled as nodal masses (marked as red in Fig. 12). Ship collision is fulfilled by giving an initial velocity of the ship mass, and the contact spring has an "infinite" stiffness in compression to mimic physical contact during collision and zero stiffness in tension to facilitate separation after collision. The ship stiffness is modelled as nonlinear springs, which are defined by force–deformation curves obtained from local collision analysis in LS-DYNA with detailed shell modelling. Finite element models of the supply vessel bow and broadside and the resulting force–deformation curves from LS-DYNA analysis are described.

3.3.1.1. Force-displacement curve for the bow of a supply vessel. Fig. 13 shows the finite element model of the bow of the supply vessel. The plate thickness varies from 7 mm for the decks to 12.5 mm in the bulb. The stiffener spacing is about 600 mm with ring stiffeners and breast hooks of approximately 250 × 15 mm in the bulb. The bulbous part is almost cylindrical and is relatively strong. The forecastle protrudes 1.2 m ahead of the bulb. The four-

Table 8
Principal dimensions of the striking vessel.

Displacement	7500 tons
Length	90 m
Breadth	18.8 m
Depth	7.6 m
Draft	6.2 m

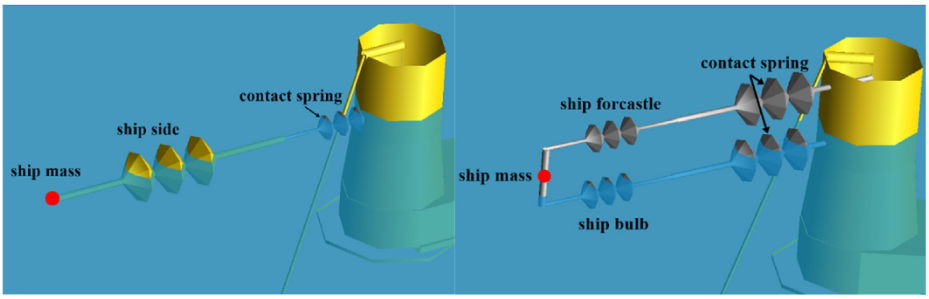

Fig. 12. The mass-spring system for ship collisions.

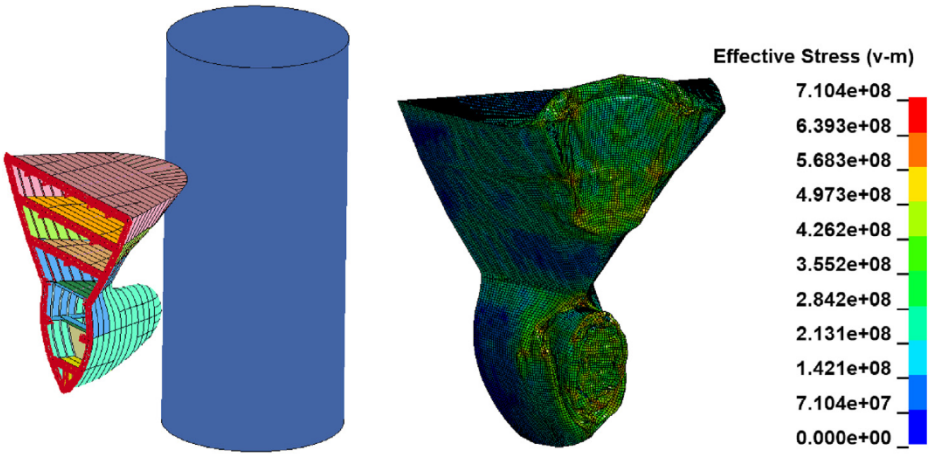

Fig. 13. The FE model of the bulbous bow, the collision scenario and bow deformation.

node Belytschko-Lin-Tsay shell element is used with a mesh size of 120 mm in general. The struck outer concrete column of the floater has a diameter of 13.4 m. The concrete column is considered to strong enough to avoid punching shear or flexural failure of the column wall and is modelled as rigid. The ship bow is fabricated in mild steel, which is assumed to have a yield stress of 275 MPa. The power law material model is used for the mild steel with the power law coefficients K = 830 MPa and n = 0.24. The RTCL criterion [24] is adopted for modelling fracture initiation and propagation of steel.

The ship bow is fixed against motions and rotations. The rigid column moves with a constant speed of 2 m/s into the ship bow. The penalty-based contact algorithms are used to model the contact between the vessel and the rigid column. A friction coefficient of 0.3 is assumed for all the contacts. The resulting force-displacement curve for the bow resistance and the fitted curves for USFOS are plotted in Fig. 14. The fitted curves follow the average values of the simulation curves and are considered reasonably accurate for energy absorption.

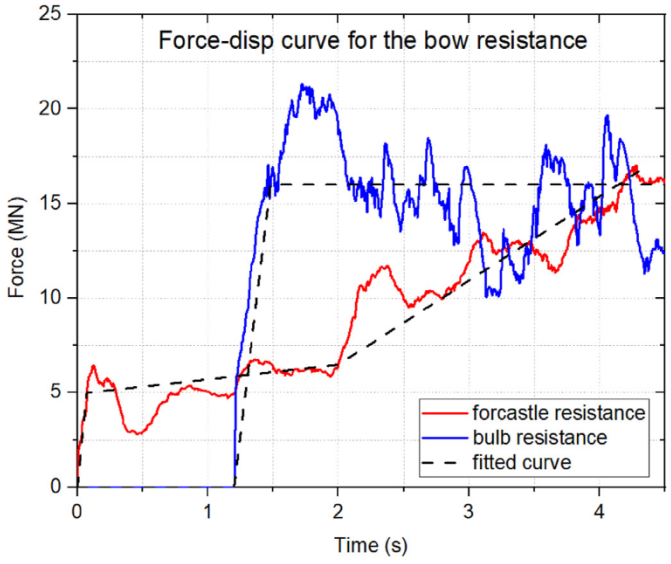

Fig. 14. Force-displacement for the crushing of supply vessel bow.

3.3.1.2. Force-displacement curve for broadside impact by a supply vessel. The vessel side model is displayed in Fig. 15 (left). The length, width and height of the segment are 15.6 m, 5.5 m and 7.6 m respectively. The ship side model is established according to the structural drawings, with shell thicknesses varying from 7.5 mm to 25 mm. The thickness of the side girders in the bilge area is 9.5 mm, and the frame spacing is 650 mm. The same steel material with a yield stress of 275 MPa is used as for the ship bow model in *Section 3.3.1*. The RTCL criterion is adopted for the prediction of steel fracture.

The boundary conditions for the ship side are defined at the longitudinal and transverse edges of the model backside as well as the fore and after edges. These edges are constrained in all rotational and translational degrees of freedom. The rigid column with a diameter of 13.4 m moves with constant velocity of 2 m/s into the ship side. The same numerical settings are used for contact and friction as for the ship bow collisions. The damage on the supply vessel side is plotted in Fig. 15 (right). The resulting force-

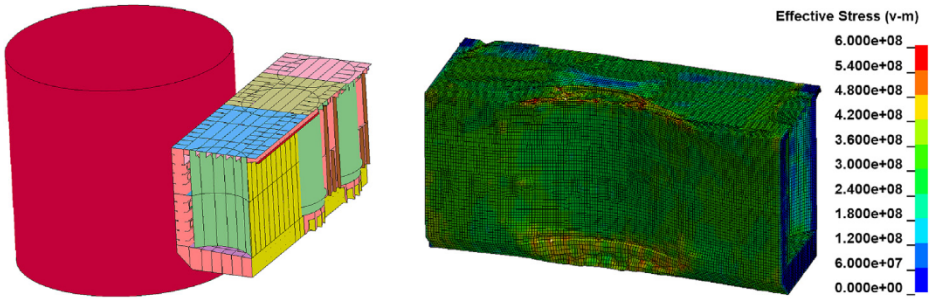

Fig. 15. The FE model of the supply vessel side, the collision scenario and ship side deformation at a indentation depth of 1.8 m.

displacement curve for the bow resistance and the fitted curves for USFOS are plotted in Fig. 16. The recommended force-displacement curve from the DNV RP C204 [25] for supply vessel side collision with a 10 m diameter rigid column is also plotted. The force levels are comparable.

3.3.2. Shuttle tanker

Offshore wind farms located close to the traffic lanes may be prone to collisions by large merchant vessels, e.g. oil tankers. A characteristic 150,000-ton shuttle tanker is selected. The length between perpendiculars of the tanker is 251 m and the tanker draft is 22.2 m. The force displacement curve for the tanker side is taken from Kjeøy and Amdahl [26] and is plotted in Fig. 17.

4. Global collision analyses in USFOS

4.1. The analysis procedure and collision scenarios

The ship-FOWT collision analysis includes both local and global structural response analysis as well as hydrodynamic and aerodynamic loads. The analysis is carried out in three steps as shown in Fig. 18.

(1) Local structural impact analysis in LS-DYNA (section 3.3).

This yields the local structural damage and provides the force-displacement curve as the input spring stiffness representing the ship stiffness in USFOS analysis.

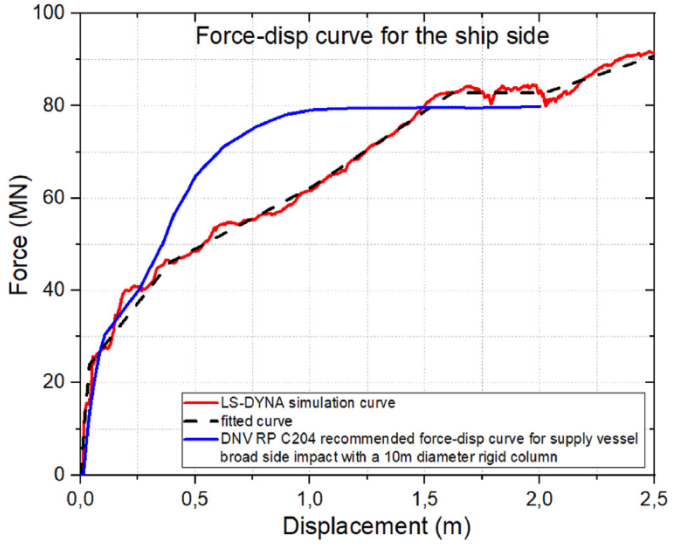

Fig. 16. Force-displacement for the crushing of the supply vessel side and the recommended curve from DNV RP C204 [25].

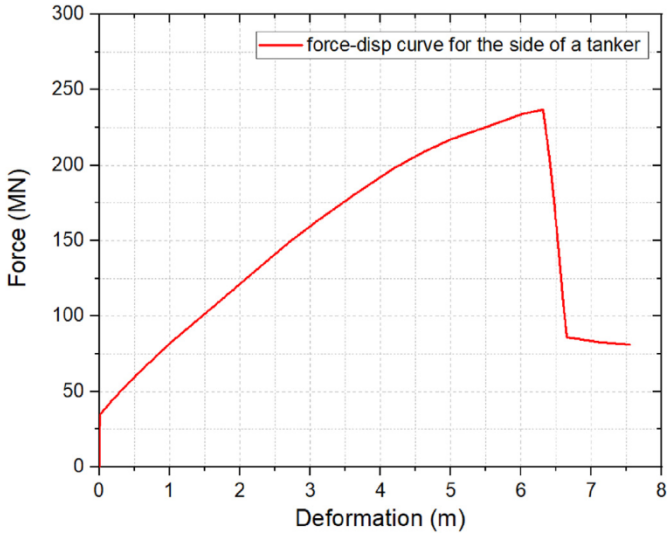

Fig. 17. Force-displacement for the side of a 150,000 tons shuttle tanker.

(2) Aerodynamic analysis using HAWC2 (section 3.2).

This gives wind thrust loads in steady state conditions under the rated wind speed. The wind loads will be applied on turbine blades as distributed line loads in USFOS.

(3) Global USFOS analysis

By utilizing the local ship stiffness and aerodynamic loads as inputs, the USFOS analysis calculates global responses of the FOWT and the ship in collisions.

The striking vessel may hit different positions of the FOWT in different directions. Due to symmetry, only columns 1 and 2 are considered, refer Fig. 19. The ship impact direction is defined as the angle relative to the rated wind direction (negative x direction). Fig. 19 shows several representative collision scenarios with different struck column and impact directions. The FOWT in both parked and operative conditions are considered.

4.2. Ship collision with the FOWT in parked condition

During weather conditions where the wind speed is below the cut-in speed or the turbine is under maintenance, the FOWT is in parked condition with stationary turbine blades. Hence, structural performance of the FOWT in parked condition under ship impacts is investigated by having stationary blades and no wind loads.

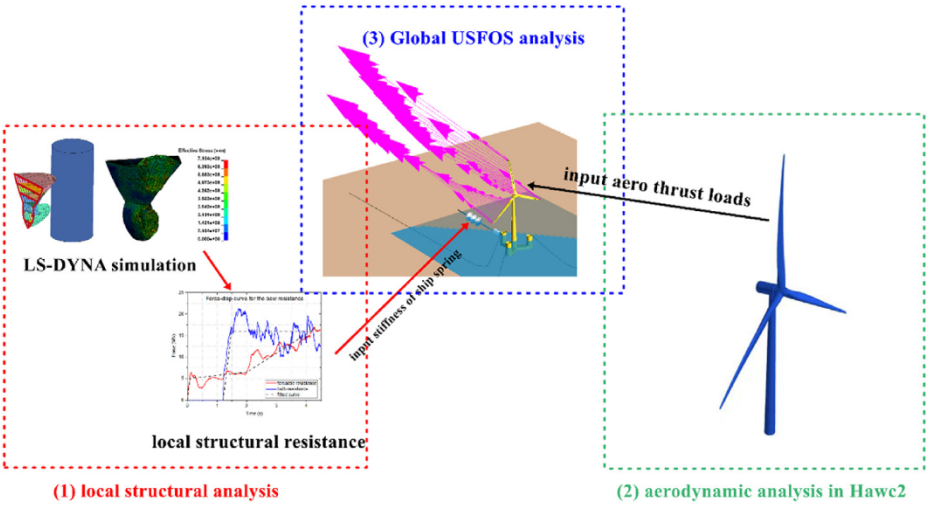

Fig. 18. The procedure for local and global analysis of ship-FOWT collisions.

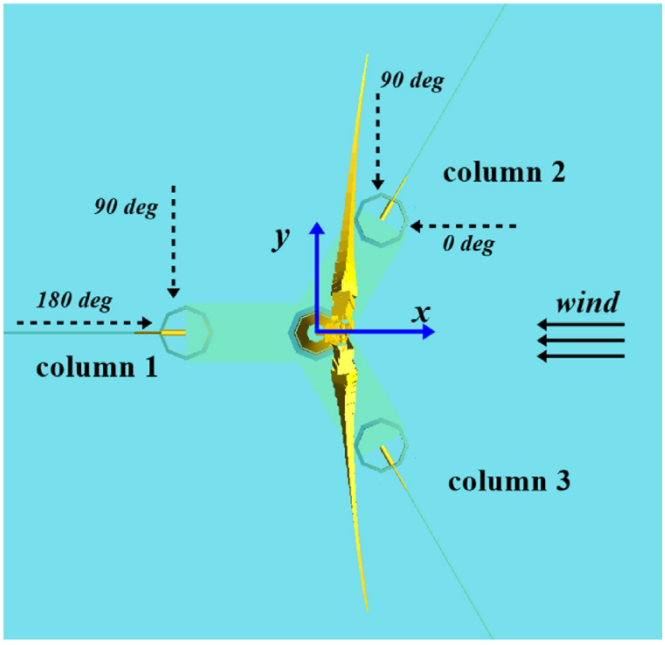

Fig. 19. Definition of the ship – FWOT collision scenarios.

Gravity and buoyancy forces are applied at the initial stage of the analysis, and ship collision occurs at 200 s when the system becomes fully stabilized.

4.2.1. Energy dissipation and ship-FOWT motions

4.2.1.1. • ***Supply vessel collisions***. Table 9 shows energy absorption of the supply vessel and the FOWT for four representative cases immediately after supply vessel bow and side collisions. Figs. 20 and 21 plot the kinetic energy in different cases and corresponding force displacement curves for the supply vessel bow and side. The extracted force-displacement curves of the bow and side from USFOS follow well the target curves, demonstrating correct implementation of the ship resistance model. Fig. 22 plots characteristic motions of the supply vessel and the FOWT during and after collisions.

For supply vessel bow collisions, a collision velocity of 3 m/s for the selected vessel yields a total energy of 37.1 MJ considering hydrodynamic effects. The total energy is 21 MJ for vessel side collisions with a design collision velocity of 2 m/s. Both the supply bow and side deform significantly in collisions and absorb considerable energy, i.e. 21.0–27.0 MJ for the supply vessel bow and 10.4–13.9 MJ for the vessel side from Table 9. Little kinetic energy remains in the supply vessel after collision in general. For the cases *column1-180deg-supply vessel bow* and *column1-180deg-supply vessel side*, the FOWT response is dominated by translatory motions. For the cases *column1-90deg-supply vessel bow* and *column1-90deg-supply vessel side*, multiple impacts are observed from the velocity plots in Fig. 22, where the yaw and sway motions of the FOWT dominate. In the two cases, after the first impact with contact separation, the ship still has a positive velocity and moves forward continuously, while the contact point of the FOWT moves forward with the excited sway and yaw velocities. The velocities decrease with time under the combined action of hydrodynamic damping and the mooring forces. A second collision occurs when the vessel meets the FOWT again. A small part of the total energy may be dissipated through vibration of the tower, structural damping, hydrodynamic damping and the mooring system.

In order to quantify the level of energy absorption due to tower vibrations after collision, we apply a nodal load statically at the tower top to the target displacement i.e. amplitude of the tower top vibrations from the dynamic collision analysis, being 0.13 m for case *column1-180deg-supply vessel bow* and 0.30 m for case *column1-180deg-supply vessel side*, and then release the load to enable free vibrations of the tower (see Fig. 23). This yields 0.28 MJ for the case *column1-180deg-supply vessel bow* and 0.70 MJ for case *column1-180deg-supply vessel side*, corresponding to 0.7% and 3.3% of the total energy, respectively. The results indicate that for ship collisions with floating offshore wind turbines, the energy carried by tower vibrations is in general limited.

4.2.1.2. • ***Shuttle tanker collisions***. In the case of shuttle tanker side collision, a velocity of 2 m/s gives an initial kinetic energy of 420 MJ including hydrodynamic added masses. Fig. 24 plots evolution of the kinetic energy of the tanker-turbine system during and after collisions and the corresponding force displacement curves. The time history of the collision force for case *column1-180deg-tanker side* is plotted as well. Figs. 25 and 26 display velocities and motions of the tanker and the floating turbine during and after collisions, respectively. Multiple impacts occur due to the large

Table 9
Energy dissipation of the supply vessel and the parked FOWT immediately after collision.

Case	column1-180-bow	column1-90-bow	column1-180-side	column1-90-side
Total energy	37.1 MJ	37.1 MJ	21 MJ	21 MJ
supply vessel strain energy	Forecastle 12.7 MJ Bulb 14.3 MJ	Forecastle 11.3 Bulb 9.7	13.9 MJ	10.4 MJ
supply vessel kinetic energy after first collision	0.1 MJ	0.7 MJ	≈0 MJ	0.8 MJ
Main motion energy of the FOWT after collision	8.7 MJ, Including: surge motion 6.3 MJ pitch motion 1.3 MJ top structure energy 1.1 MJ	12.8 MJ, Including: sway motion 4.1 MJ Yaw motion 6.7 MJ Roll motion 1.0 MJ top structure energy 1.0 MJ	6.54 MJ, Including: surge motion 4.6 MJ pitch motion 1.0 MJ top structure energy 0.94 MJ	8.7 MJ, Including: sway motion 2.8 MJ Yaw motion 4.3 MJ Roll motion 0.7 MJ top structure energy 0.9 MJ
Others	1.4 MJ	3.3 MJ	0.56 MJ	1.1 MJ

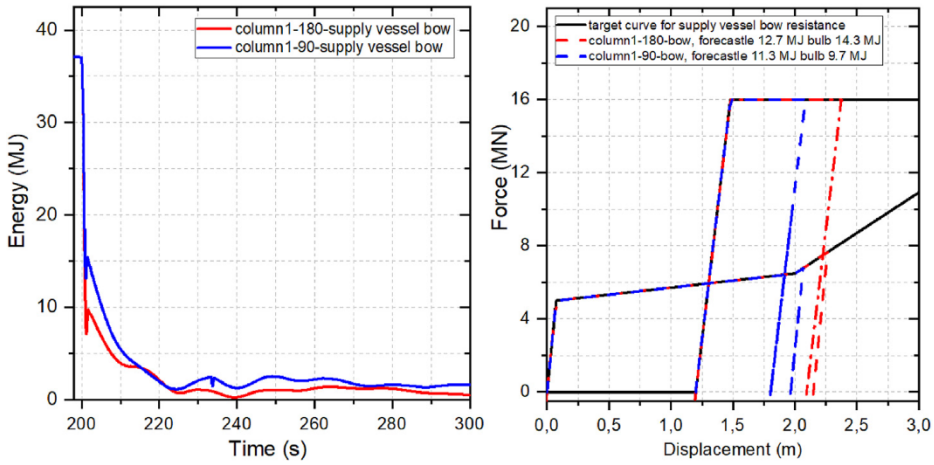

Fig. 20. (left) Kinetic energy of the supply vessel bow-parked FWOT system during and after collision; (right) Force-displacement curves of the supply vessel forecastle and bulb in collisions.

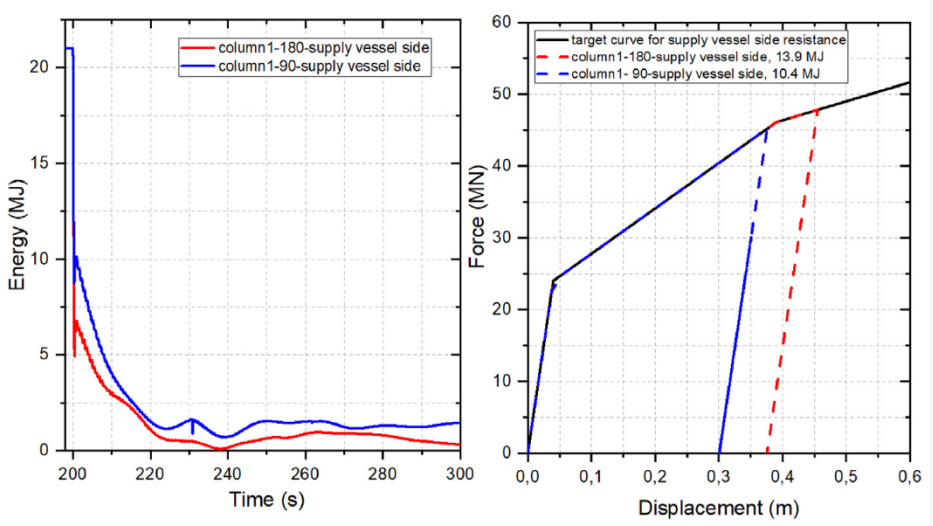

Fig. 21. (left) Kinetic energy of the supply vessel side-parked FWOT system during and after collision; (right) Force-displacement curves of the supply vessel side in collisions.

mass of the shuttle tanker and the induced periodic motions of the FOWT. The peak collision force reaches a maximum value in the first impact and decreases afterwards in the consecutive impacts, so the repeated impacts after the first are considered to fall in the elastic loading/unloading range in USFOS. Therefore, only the first impact governs the damage in terms of plastic deformations as well as the maximum force.

For the case *column1-180deg-tanker side*, the tanker dissipates 58.9 MJ by plastic deformation after the first major impact with a deformation of 1.0 m and a maximum force of 81 MN. The floating turbine absorbs 49.1 MJ through the surge motion. The turbine is pushed to a maximum surge displacement of 61 m before the

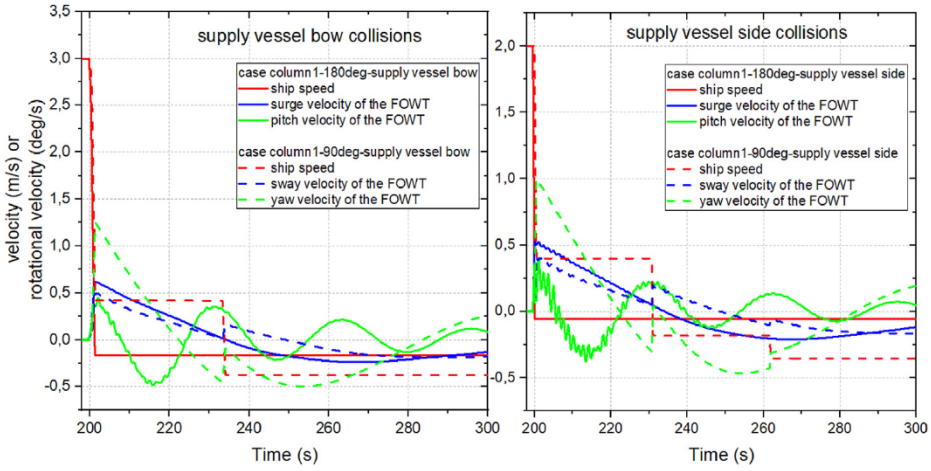

Fig. 22. Motions of the ship and the parked OO-STAR floating turbine during and after (left) supply vessel bow collisions and (right) side collisions.

mooring lines pull the FOWT back, and a maximum pitch motion of 8.6°. The masses of the top structure including the nacelle and rotor carry a kinetic energy of 8.4 MJ. The energy carried by the tower vibrations is still small, about 1.6 MJ.

For the case *column2-0deg-tanker side* where the yaw motion of the FOWT is significant, the tanker dissipates 30.5 MJ by structural deformation after the first impact. The floating turbine absorbs 13.8 MJ through the surge motion and 16.3 MJ through the yaw motion. The turbine is pushed to a maximum surge displacement of 82 m before the mooring lines pull the FOWT back, and a maximum yaw motion of 45°. The mass of the top structure including the nacelle and rotor carries a kinetic energy of 3.4 MJ.

4.2.2. Nacelle acceleration

It is common industrial practice for designing floating wind turbines to set an operational limit for the tower-top axial acceleration, normally in the range of 0.2–0.3 g, which is typically understood to be related to the safety of delicate mechanical and electrical equipment in the nacelle. Fig. 27 plots accelerations of the nacelle for several representative collisions from the supply vessel bow and side. The maximum nacelle accelerations are 0.21 g for supply vessel bow collisions and 0.44 g for supply vessel side collisions, both of which exceed the allowable operational limit. The acceleration is especially serious for the supply vessel side collisions with significant exceedance. This indicates that supply vessel collision loads are critical to the safety of the turbine nacelle. Multiple impacts are observed from the performance of nacelle accelerations due to the excited periodic motions of the FWOT. The forces and resulting consequences of secondary impacts are however much less severe than those of the first impact.

For tanker side collisions, the nacelle acceleration plotted in Fig. 28 is even larger with a maximum value of 6.9 m/s^2. This exceeds significantly the operational limit and may cause damage to the nacelle. Several acceleration peaks indicate the occurrence of multiple impacts.

4.2.3. Tower clearance

The tower clearance i.e. the distance of the blade tip to the tower, is more critical in operative conditions when wind loads are applied. The tower clearance is therefore not discussed for the FOWT in parked conditions.

4.2.4. Tower bending moment

The turbine tower is an unstiffened cylindrical shell with varying diameters and thicknesses from the bottom to the top. The tower is made of steel with a yield stress of 355 MPa. The tower is subjected to bending stresses due to collision induced vibrations and axial compression from gravitational loads, and thus shall be designed against local buckling.

According to DNV RP C202 [27], the elastic buckling strength of an unstiffened cylindrical shell σ_E is given by:

$$\sigma_E = C\frac{\pi^2 E}{12(1-\nu^2)}\left(\frac{t}{l}\right)^2 \tag{2}$$

where t is the shell thickness, l is the length of the member, E and ν are the Young's modulus and the Poisson ratio, respectively.

The reduced buckling coefficient C may be calculated as:

$$C = \psi\sqrt{1+\left(\frac{\rho\xi}{\psi}\right)^2} \tag{3}$$

The values for ψ, ξ and ρ are given in Table 10 for the most important load cases, and the curvature Z_l is defined as:

$$Z_l = \frac{l^2}{rt}\sqrt{1-\nu^2} \tag{4}$$

The knock-down factor for shape imperfections is essential both in the elastic and elastoplastic range. Modifying the elastic critical stress for plasticity is achieved by calculating the characteristic buckling strength. The critical stress is defined by

$$\sigma_{eq,cr} = \frac{\sigma_y}{\sqrt{1+\bar{\lambda}_{eq}^4}} \tag{5}$$

The equivalent slenderness parameter $\bar{\lambda}_{eq}^2$ is given as,

$$\bar{\lambda}_{eq}^2 = \frac{\sigma_y}{\sigma_{eq,E}}\left[\frac{\sigma_{x,sd}}{\sigma_{xE}}+\frac{\sigma_{b,sd}}{\sigma_{bE}}+\frac{\tau_{sd}}{\tau_E}\right] \tag{6}$$

$\sigma_{x,sd}$ is the design axial stress, $\sigma_{b,sd}$ is the design bending stress, and τ_{sd} is the design shear stress.

The utilization factor η is a measure of the ratio between the equivalent stress and the critical equivalent stress. This factor should be smaller than one in order to have an adequate design

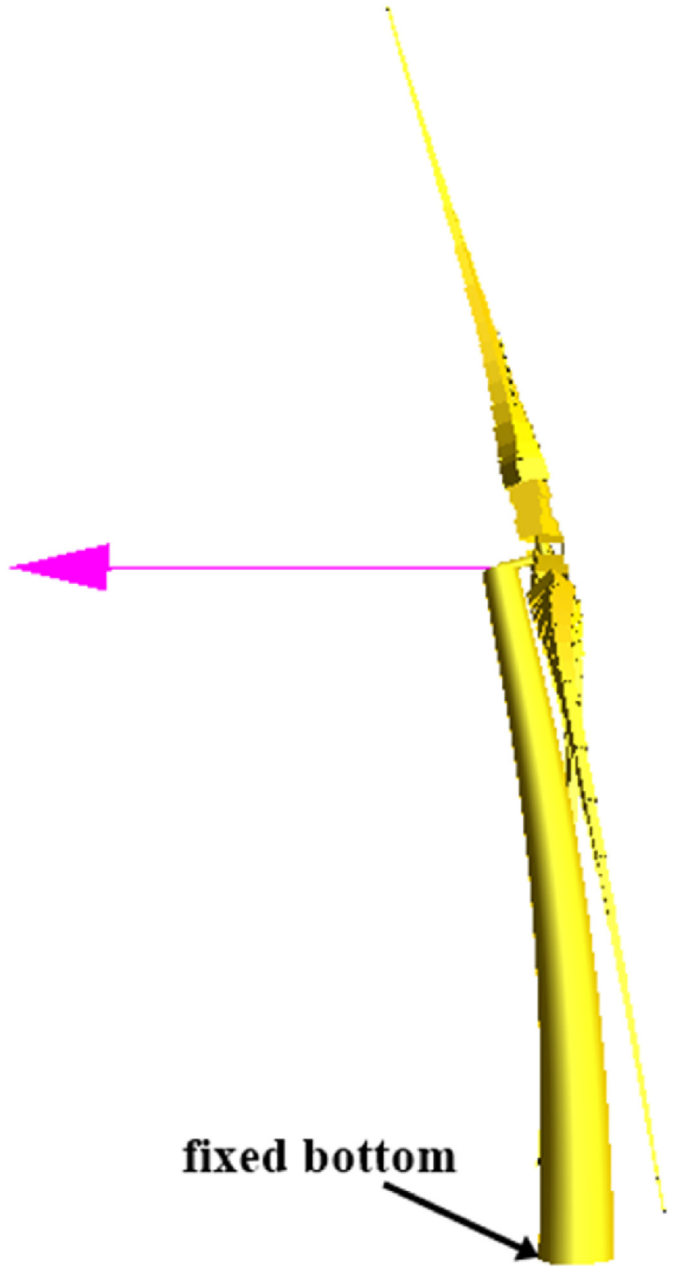

Fig. 23. Energy absorption of the turbine tower and blades when the tower top is loaded statically to a certain displacement and then released to enable free vibrations. (the displacement is magnified by 100 times for visual purpose).

with respect to the elastoplastic buckling of the tower.

$$\eta = \frac{\gamma \sigma_{eq}}{\sigma_{eq,\,cr}} \tag{7}$$

Here, we consider conservatively the material factor to be $\gamma = 1.45$.

Based on the above equations and dimensions of the turbine tower, the slenderness ratio for the turbine tower is calculated to be in the range $0.30 < \bar{\lambda}_{eq}^{2} < 0.42$ along the tower. This indicates that the tower cross section is relatively compact.

Fig. 29 shows the maximum stress and the corresponding buckling utilization factor of the cross sections along the turbine tower induced by collisions from the supply vessel side and tanker side, which are considered the worst case for the tower. The utilization factor is small for supply vessel side collisions with significant safety margin against local buckling of the tower wall. As we have selected a conservative material factor of 1.45 already, all utilization factors below 1 are considered adequate. For tanker side collisions, the utilization factor is in the range of 0.75–0.82, which gives considerable safety margin as well. The turbine tower has varied thicknesses and diameters along the height. Contrary to our intuition, the maximum stress does not occur at the bottom of the tower, but at the top half of the tower. This needs to be considered in the design of wind turbine towers.

4.3. Ship collision with the FOWT in operation conditions

Ship collisions are a risk also for operating wind turbines with rotating turbine blades and wind thrust forces. In the collision analysis with the operating FOWT, buoyancy and gravitational loads are applied at the initial stage. Wind thrust loads and moments for blade rotation are applied at 70 s, and the FOWT is then gradually pushed away to a displacement of 33 m (refer to Fig. 30) when the wind thrust is balanced by the mooring system. Under the action of wind thrust at the rated wind speed, the FOWT has a steady negative pitch angle of 5.8° in operating conditions, see Fig. 30. Ship collision is assumed to occur at 400 s after stabilization of the system. The collision scenarios are defined in *Section 4.1*.

4.3.1. Energy dissipation and ship-FOWT motions

4.3.1.1. • ***Supply vessel collisions***. Fig. 31 plots the kinetic energy with operating turbines in different collision cases from the supply vessel bow and side, and the corresponding force displacement curves. Energy absorption of the supply vessel and the OO-STAR floating wind turbine for the four representative cases immediately after collisions is summarized in Table 11. Fig. 32 plots velocities of the characteristic motions of the supply vessel and the turbine during and after collisions.

The results show that for supply vessel bow collisions, the distribution of energy absorption in the forecastle and the bulb is quite different with the turbine in parked condition because of the turbine pitch motion under wind thrust. Fig. 33 plots an example of the temporal evolution of the pitch motion for the case *column1-180deg-supply vessel bow*. With the buoyancy and gravity loads applied, the turbine has a small initial pitch angle of about 0.7°due to offset of the rotor. When wind loads are applied, the turbine reaches a steady pitch angle of about −5.8° in operation conditions. This changes the relative distance of the bulb and the forecastle to the platform, yielding different energy distribution in the forecastle and bulb compared to that in parked condition. More energy goes into the bulb when the collision is in line with the wind direction. Conversely, when the supply vessel collides from the opposite wind direction, the ship forecastle dissipates more energy.

Generally, the energy absorption modes do not differ much from collisions with the turbine in parked conditions. Both the supply vessel bow and side deform significantly and absorb considerable energy, i.e. 22.3–27.2 MJ for the ship bow and 11.5–14.2 MJ for the ship side from Table 11. Limited kinetic energy remains in the ship after collision. The FOWT dissipates energy mainly through motions of turbine floater and the top structure. The rest of the energy is dissipated through vibration of the tower, structural damping, hydrodynamic damping and the mooring system. The energy dissipated by vibrations of the tower is small in general.

4.3.1.2. • ***Shuttle tanker collisions***. For the shuttle tanker collision with the OO-STAR FOWT in operating conditions, the initial pitch angle of the floater due to wind loads makes the platform vulnerable to the risk of capsizing. For the case *column1-180deg-tanker*

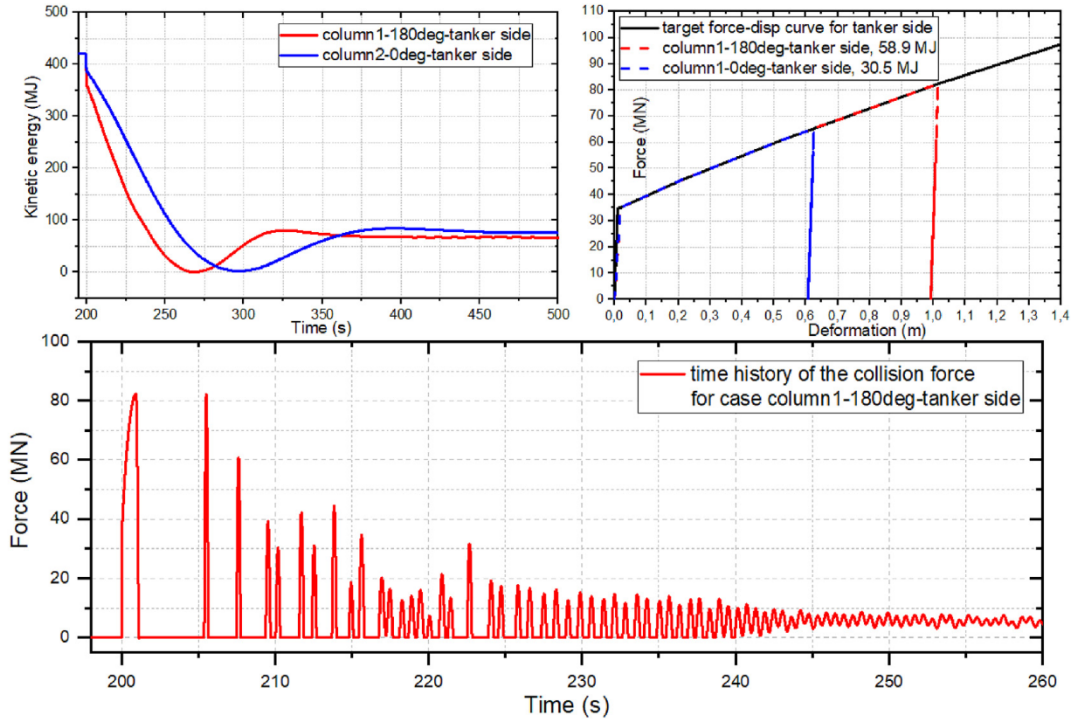

Fig. 24. (top left) Kinetic energy of the shuttle tanker side-parked FWOT system during and after collision; (top right) Force-displacement curves of the shuttle tanker side in collisions; (below) the time history of collision forces for the case column1-180deg-tanker side with multiple impacts.

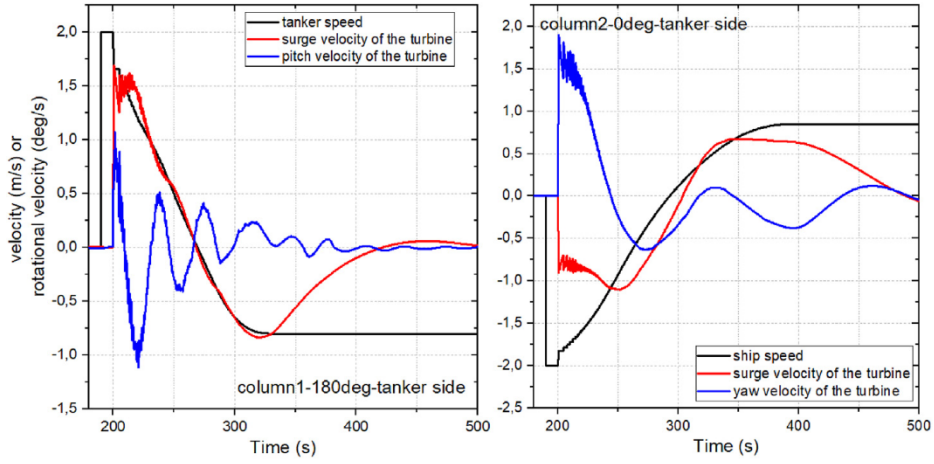

Fig. 25. Velocity of the tanker and the turbine during and after collisions.

side in operating condition, the whole platform overturns under the combined action of collision loads, wind thrust loads and mooring forces as shown in Fig. 34. The tanker collision starts at t = 400 s, and due to the large mass and kinetic energy of the tanker, the FOWT is continuously pushed away with increasing pitch and surge motions. At t = 453 s as shown in Fig. 34(left), the contact force decreases to zero, i.e. the collision terminates, but the FOWT moves forward continuously with imparted velocities. The FOWT undergoes increasing pitch motion until the platform loses its hydrostatic stability and overturns eventually. The mooring line on the striking vessel side is significantly tightened, while the other two mooring lines unload and thus lose their capabilities to pull the turbine upright. This demonstrates the significant risk of platform overturning should the FOWT be collided by large passing shuttle tankers.

4.3.2. Nacelle acceleration

Fig. 35 plots nacelle accelerations for the OO-STAR floating turbine in operative conditions subjected to collisions from the supply vessel bow and side. The selected scenarios represent ship collisions along the wind direction and opposite to the wind direction, respectively. The plots show that the nacelle accelerations exceed the maximum allowable operation limit, i.e. 0.2–0.3 g, especially for the side collisions. This is consistent with observations for collisions with the turbine in parked condition. It is noted that nacelle accelerations are somewhat reduced when the vessel hits from the opposite wind direction and are magnified to some extent for collisions in line with the wind direction. Nacelle

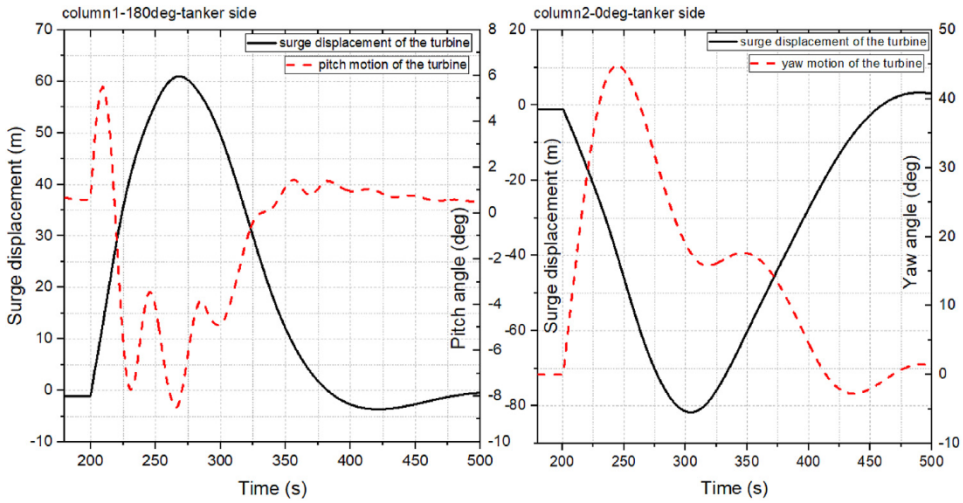

Fig. 26. Motions of the OO-STAR floating turbine during and after tanker collisions.

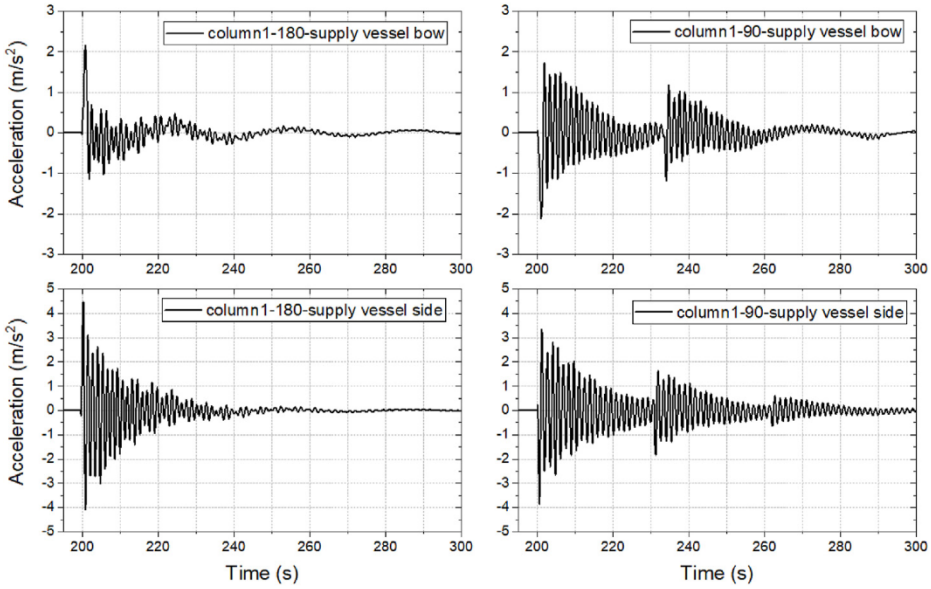

Fig. 27. Acceleration of the turbine nacelle during and after supply vessel bow and side collisions.

accelerations for the tanker collisions are not presented due to capsizing of the FOWT in operative condition, but the values are comparable to those in the cases with parked turbines.

4.3.3. Tower clearance

The maximum blade tip deflection is an important design parameter, and the blades must be kept at a safe distance from the turbine tower. For that matter, the blades often have a prebend, the rotor has a precone angle and the shaft is tilted. All these effects increase the tower clearance. It is crucial to monitor the clearance during an accidental ship collision as the consequence of an impact between the turbine tower and the blade can be severe, causing repair downtime and economic losses.

The tower clearance can be reduced by bending and vibration of the turbine blades and bending of the tower. Fig. 36 plots the displacement of the blade tip relative to its undeformed position for the four representative collision cases from supply vessel bow and side, and the cases are considered to give the worst conditions of the tower clearance for the supply vessel bow and side impacts. From Fig. 36, the turbine blade yields a deflection of about 6.8 m at the rated wind speed of 11.4 m/s. When collision occurs, the turbine blade starts to vibrate, yielding a maximum blade tip deflection of 8.25 m for supply vessel bow collision from the opposite wind direction and 8.58 m for bow collision from in line with the wind direction. For supply vessel side collisions, the maximum blade tip deflection is 9.26 m for collisions from the opposite wind direction and 9.73 m for collisions from in line with the wind direction. This indicates that it is more dangerous for the reduction of tower clearance when the vessel direction aligns with the wind direction.

Bending vibration of the turbine tower may also contribute to decreasing the tower clearance. The maximum vibration amplitude of the tower top is 0.33 m for the case *column1-180deg-supply vessel bow* and 0.44 m for case *column1-180deg-supply vessel side*. This has very small influence on the tower clearance, i.e. less than 0.4 m deflection of the blade tip. Considering a total tower clearance of 16.5 m, the studied FOWT has sufficient margins to avoid collision between blades and the tower for supply vessel collisions. For the shuttle tanker collisions, the tower clearance is slightly larger than

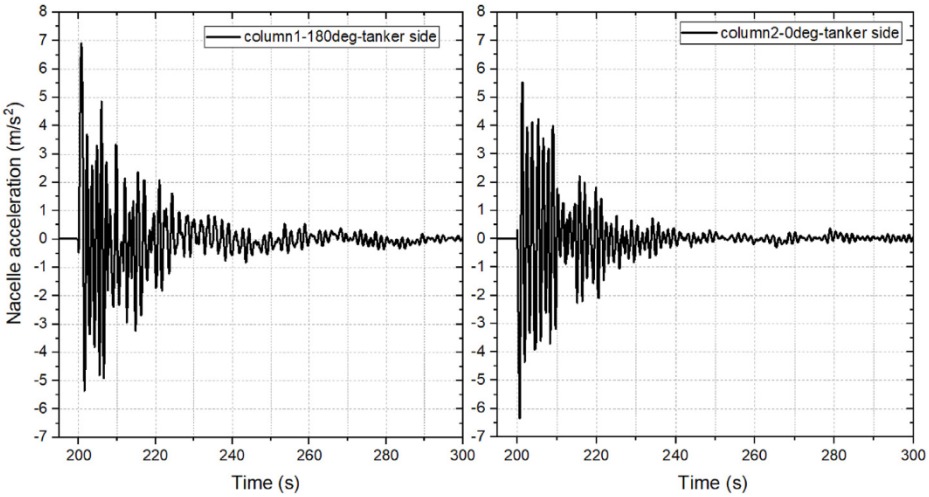

Fig. 28. Acceleration of the turbine nacelle during and after tanker side collisions.

Table 10
buckling coefficients for unstiffened cylindrical shells.

	Ψ	ξ	ρ
Axial stress	1	$0.702Z_l$	$0.5\left(1+\frac{r}{150t}\right)^{-0.5}$
Bending	1	$0.702Z_l$	$0.5\left(1+\frac{r}{300t}\right)^{-0.5}$
Torsion and shear force	5.34	$0.856\ Z_l^{3/4}$	0.6

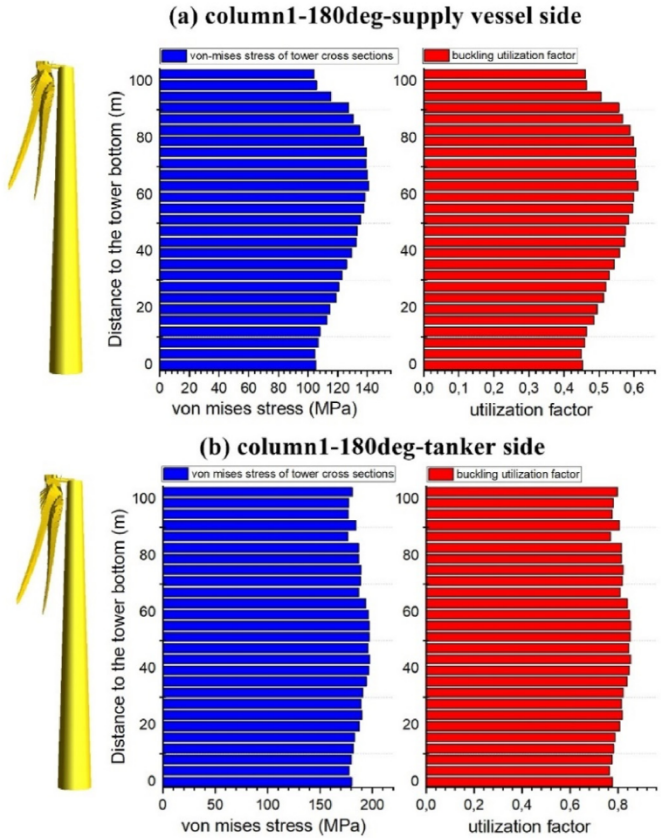

Fig. 29. Buckling assessment of the turbine tower.

that in supply vessel side collisions but is in general safe against the risk of blade and tower collisions.

It should be noted that the above assessment is based on ship collisions with the design collision velocities, i.e. 3 m/s for bow collisions and 2 m/s for side collisions. If the ship impact velocity increases, the tower clearance will be further reduced.

4.3.4. Tower bending moment

Fig. 37 shows the von-mises equivalent stress and buckling utilization factors of cross sections along the turbine tower when the supply vessel side collides with the operative FOWT. Wind thrust loads increase notably the bending moments along the tower and introduce a shear stress across the tower cross section. The buckling utilization factor increases compared to the same collision scenario with the parked turbine. The values are however still smaller than 0.8, and there is still considerable safety margin remaining against local tower buckling. The tower bending moment of the operative turbine under shuttle tanker collision is not discussed due to capsizing of the platform.

4.3.5. Mooring forces

The platform mooring lines may be significantly stretched during and after ship collisions and should be checked against possible mooring line breakage. The condition becomes especially critical when the striking ship and the FOWT are locked together after impact. It is interesting to examine whether or not the mooring lines are capable of stopping the moving bodies.

In order to check the capacity of the mooring lines, the FOWT in both parked and operating conditions are loaded with linearly increasing nodal loads on the column 1 of the FOWT in the direction opposite to the wind. For this scenario, only one mooring line is taking up major additional forces, and it is considered the most severe case. The force-displacement curves of the mooring lines are plotted in Fig. 38. The FOWT is shown to capsize when the force of the leading mooring line reaches about 8.0 MN for collision with operating turbines and 23.0 MN for collision with parked turbines. According to DNV OS E302 [28], the proof and breaking loads of the mooring chain are calculated in Table 12 with two material grades, representing low and high strength materials, respectively. The proof load is defined as the maximum tensile force applied to the mooring chain that will not show signs of defects and plastic deformation. In other words, the material must remain in the elastic region when loaded up to its proof load. For collision with

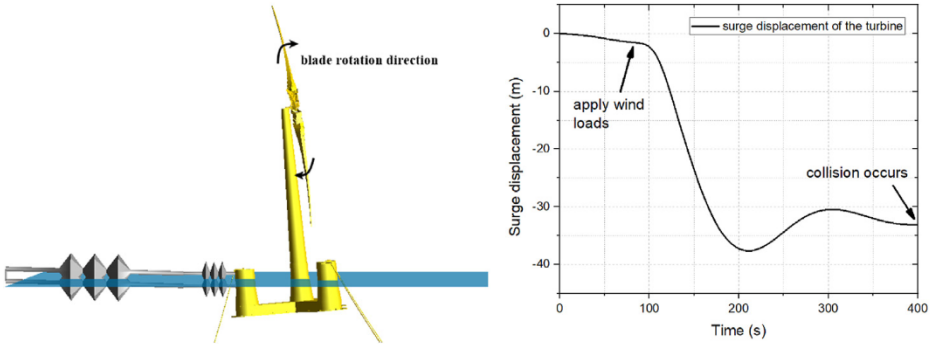

Fig. 30. Pitch motion of the OO-STAR floating turbine after stabilization of the system in operating conditions.

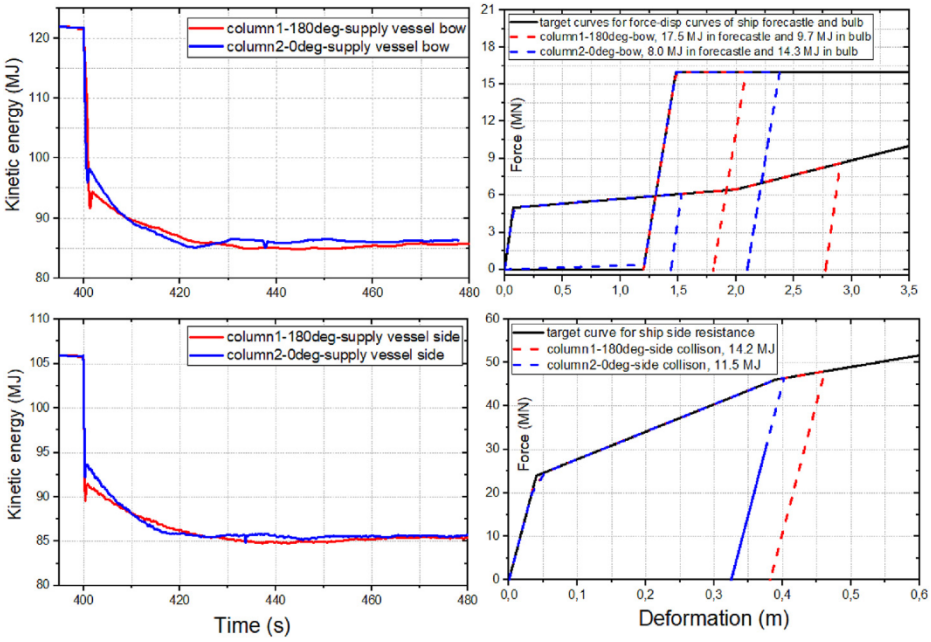

Fig. 31. Kinetic energy of the supply vessel bow-operating FWOT system during and after collision; (right) Force-displacement curves of the supply vessel bow in collisions.

Table 11
Energy dissipation of the supply vessel and the operating FOWT immediately after collision.

Case	column1-180deg- supply vessel bow	column2-0deg- supply vessel bow	column1-180deg- supply vessel side	column2-0deg- supply vessel side
Total energy	37.1 MJ	37.1 MJ	21 MJ	21 MJ
Ship deformation energy	Forecastle 17.5 MJ Bulb 9.7 MJ	Forecastle 8.0 Bulb 14.3	14.2 MJ	11.5 MJ
Ship kinetic energy after first impact	0.2 MJ	0.3 MJ	≈0 MJ	0.4 MJ
Main motion energy of the FOWT after collision	8.4 MJ, Including: surge motion 6.7 MJ pitch motion 0.7 MJ top structure energy 1 MJ	11.8 MJ, Including: surge motion 4.3 MJ yaw motion 5.7 MJ Pitch motion 0.9 MJ top structure energy 0.9 MJ	6.7 MJ, Including: surge motion 4.9 MJ pitch motion 0.8 MJ top structure energy 1.0 MJ	7.7 MJ, Including: surge motion 3.1 MJ Yaw motion 3.6 MJ Pitch motion 0.5 MJ top structure energy 0.5 MJ
Others	1.3 MJ	2.7 MJ	0.1 MJ	1.4 MJ

the operating wind turbine, the mooring line is quite stiff against breakage before the platform capsizes. For collision with parked wind turbines, the mooring line breaks before the platform capsizes.

From the USFOS simulations, the maximum mooring force is 2.4 MN for supply vessel side collisions. This indicates that the mooring system is generally not a problem in supply vessel collisions. For shuttle tanker collision with an initial kinetic energy of 420 MJ, the maximum mooring force is 7.4 MN for the parked turbine. This is smaller than the breaking load of the mooring chain. For tanker collisions with the operating turbine, the FOWT capsizes before any limit load of the mooring chains is reached.

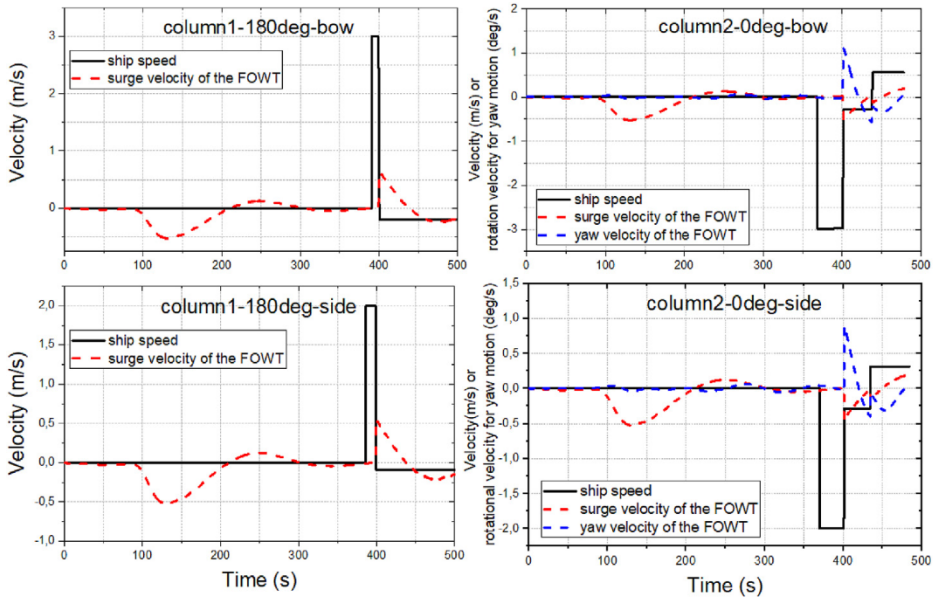

Fig. 32. Motions of the supply vessel and the operating OO-STAR turbine during and after bow and side collisions.

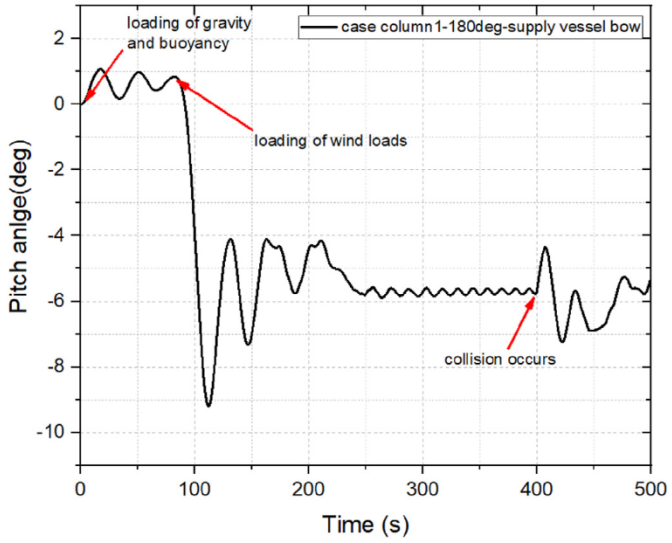

Fig. 33. Pitch angle of the operating OO-STAR turbine for case column1-180deg-supply vessel bow.

5. Discussions on strain energy dissipation

The strain energy dissipated in ship collisions is often calculated in the assessment of external dynamics. The simple equations proposed by Popov et al. [29] are adopted for illustration in this paper. In the general case, considering collisions normal to a defined impact plane, the dissipated energy will have contributions due to relative motions tangential and normal to the impact plane. Disregarding the energy dissipated by tangential "friction" energy, the energy dissipated in normal direction may be obtained as follows

$$E_S = \frac{1}{2}\overline{m}_s \bar{v}_s^2 \frac{\left(1-\frac{\bar{v}_i}{\bar{v}_s}\right)^2}{1+\frac{\overline{m}_s}{\overline{m}_i}} \tag{8}$$

where $\bar{v}_s$ and $\bar{v}_i$ are the velocity of the ship and installation, respectively, taken normal to the impact plane. In most cases, the velocity of the installation can be disregarded, i.e. $\bar{v}_i = 0$. The equivalent mass, $\overline{m}_j$, for the ship and the installation, respectively, depends on the mass, $\overline{m}_{jx}$, $\overline{m}_{jy}$, $\overline{m}_{jz}$, and the moment of inertia $\bar{I}_{jx}$, $\bar{I}_{jy}$, $\bar{I}_{jz}$, about the three axes of the coordinate system including hydrodynamic added masses, all projected on the collision plane and is given by Popov et al. [29].

$$\overline{m}_j = \left(\frac{l_j^2}{\overline{m}_{jx}} + \frac{m_j^2}{\overline{m}_{jy}} + \frac{n_j^2}{\overline{m}_{jz}} + \frac{\lambda_j^2}{\bar{I}_{jx}} + \frac{\mu_j^2}{\bar{I}_{jy}} + \frac{\nu_j^2}{\bar{I}_{jz}}\right)^{-1}, \quad j = s \text{ (ship) and } j = i \text{ (installation)} \tag{9}$$

The collision point is described by the three coordinates (x_j, y_j, z_j) relative to the center of gravity for the installation and the ship. l, m, n are the direction cosines for the unit vector normal to the collision plane (pointing outwards) where the location of the contact point is expressed in the two local coordinate systems.

$$P\left(x_j, y_j, z_j\right), \quad \mathbf{l}_j = l_j\mathbf{i} + m_j\mathbf{j} + n_j\mathbf{k}, \quad j = s \text{ (ship) and } j = i \text{ (installation)} \tag{10}$$

The lever arms for roll, pitch and yaw motions are given by

$$\begin{aligned} \lambda_j &= mz_j - ny_j, \quad j = s \text{ (ship) and } j = i \text{ (installation)} \\ \mu_j &= nx_j - lz_j \\ \nu_j &= ly_j - mx_j \end{aligned} \tag{11}$$

By substitution of the corresponding parameters from USFOS models into the equations, we obtain the dissipated strain energy

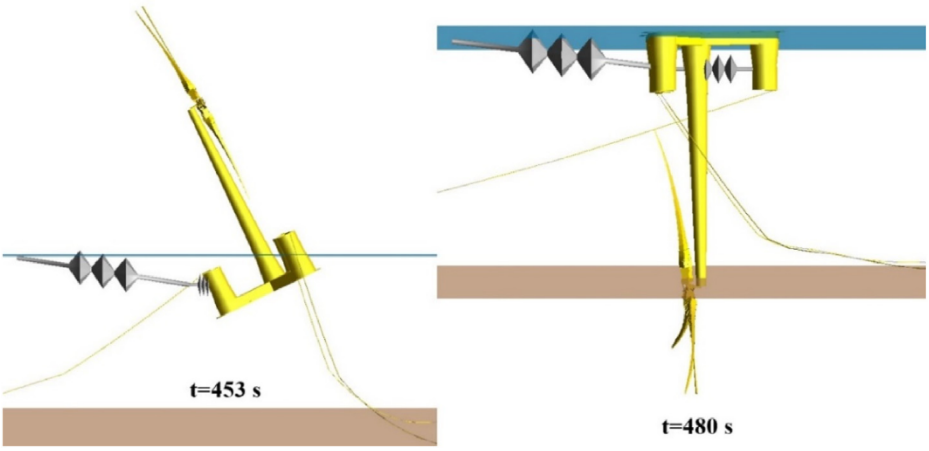

Fig. 34. Overturn of the OO-STAR floating turbine after tanker collision for the case column1-180deg-tanker side.

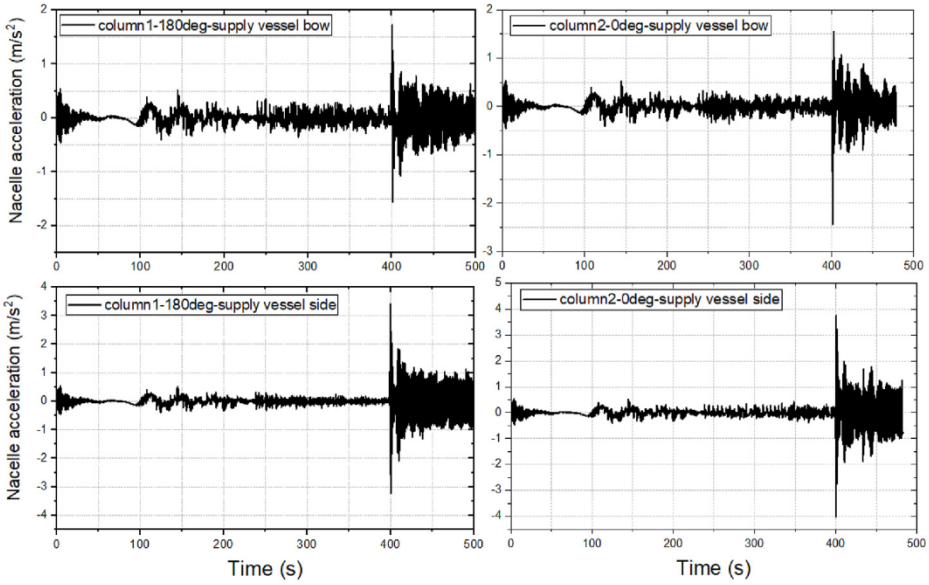

Fig. 35. Nacelle accelerations for supply vessel collisions in operation conditions.

predicted by the analytical model for the simulated cases. The predicted energy is compared with those from USFOS simulations in Table 13. The results show that the energy predicted by the simple equations agrees quite well with the strain energy from USFOS simulations; the error is within ±15% in general. In addition, in a study by Pedersen [5], where an analytical solution was proposed for the energy absorption of ship collision with bottom fixed offshore wind turbines, structural flexibilities of the tower may significantly reduce energy absorption and structural damage for bottom fixed turbines. For the studied floating turbine, the turbine tower is very stiff and the effect of tower flexibilities on structural damage is quite limited.

For a better illustration of applying the simple formulas to assess energy dissipation in ship collisions, the two cases for tanker collisions with the FOWT in parked conditions are taken as examples. The moments of inertial for the roll, pitch and yaw motions of the FOWT are $(\bar{I}_{ix} = 3.8\times10^{10},\ \bar{I}_{iy} = 3.8\times10^{10},\ \bar{I}_{iz} = 2.8\times10^{10};\ \text{unit: } kg\cdot m^2)$ considering hydrodynamic effects. This yields the radii of gyration of $(\bar{r}_{ix} = 33.4,\ \bar{r}_{iy} = 33.4,\ \bar{r}_{iz} = 28.7;\ \text{unit: } m)$ for roll, pitch and yaw motions.

For the case column2-0deg-tanker side, the collision scenario is illustated in Fig. 39. The position of the contact point in the local FOWT coordinate is $(x_i = 18.5,\ y_i = 32,\ z_i = 6.4)$. $\boldsymbol{\mu_i} = 32$ m and $\boldsymbol{\nu_i} = 6.4$ m represent the levers for the yaw and pitch motions, respectively. From eq. (9), the expression for calculating the equivalent mass of the FOWT becomes $\overline{m}_i = \left(\frac{1}{\overline{m}_{ix}} + \frac{\mu_i^2}{\bar{I}_{iy}} + \frac{\nu_i^2}{\bar{I}_{iz}}\right)^{-1} = \overline{m}_{ix}\left(1 + \left(\frac{\mu_i}{r_{iy}}\right)^2 + \left(\frac{\nu_i}{r_{iz}}\right)^2\right)^{-1}$. This indicates it is *the square of the lever over radius of gyration ratio* that governs the contributions of the associated motion to the equivalent mass, and subsequently the energy absorption. For the studied case, we obtain $\left(\frac{\mu_i}{r_{iy}}\right)^2 = \left(\frac{6.4}{33.4}\right)^2 = 0.037$ for the pitch motion, $\left(\frac{\nu_i}{r_{iz}}\right)^2 = \left(\frac{32}{28.7}\right)^2 = 1.24$ for the yaw motion, and 1.0 for the surge. Therefore, the yaw, surge and pitch motions contribute 54.4%, 44.0% and 1.6% to the total energy absorption, respectively. The resulting predicted strain energy dissipation is 27.8 MJ versus 30.5 MJ

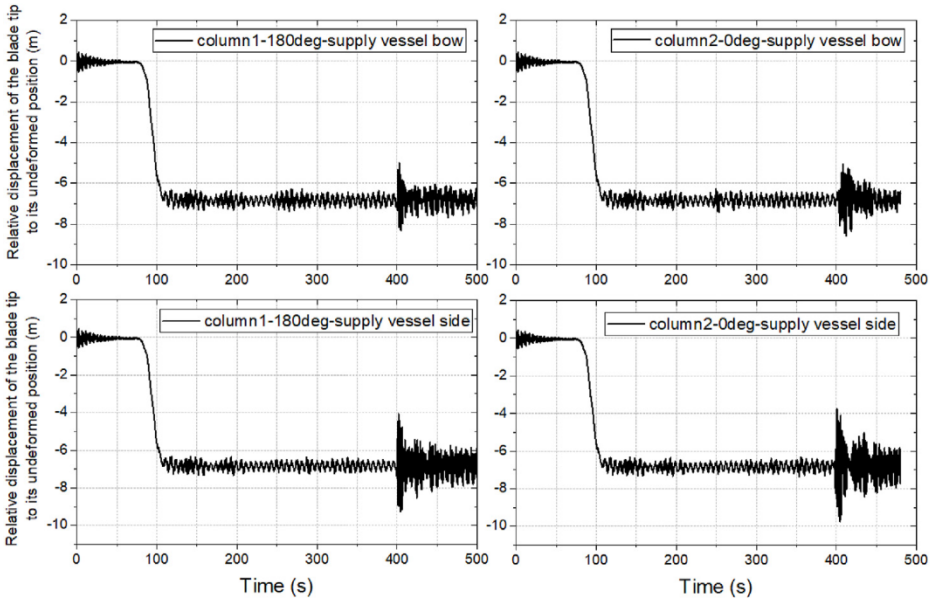

Fig. 36. Displacement of the blade tip relative to its undeformed state for case column1-180deg-supply vessel bow and column1-180deg-supply vessel side in operation conditions.

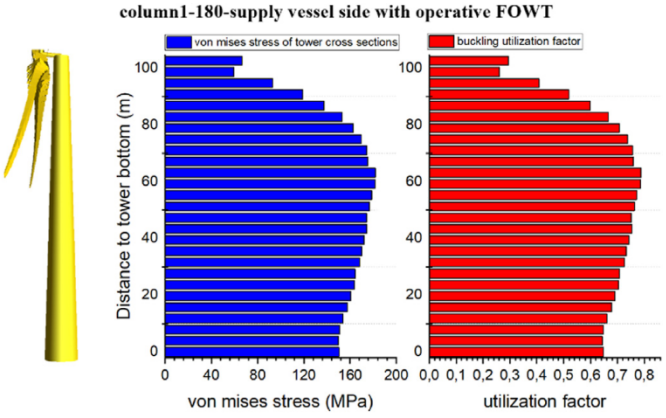

Fig. 37. Buckling assessment of the turbine tower in the collision with operating FOWT for the case column1-180deg-supply vessel side.

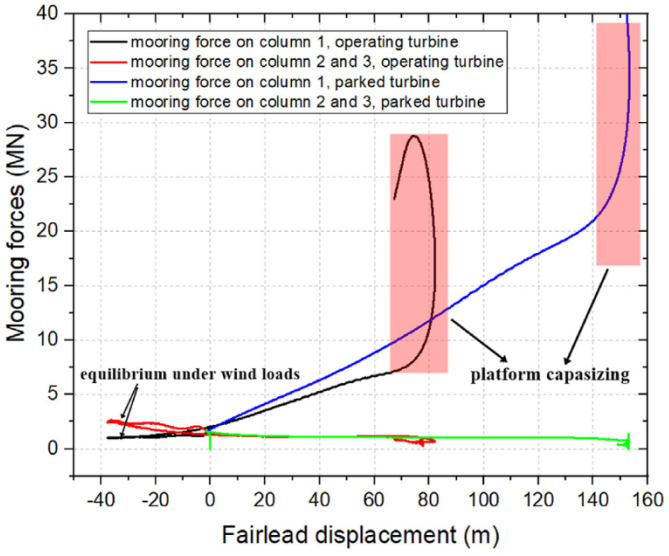

Fig. 38. Mooring loads of the FOWT subjected to nodal loads in the opposite wind direction.

from USFOS simulation, which shows reasonable agreement.

For the case *column1-180deg-tanker side*, the contact point in the local FOWT coordinate is $(x_i = -43.7,\ y_i = 0,\ z_i = 6.4)$. Similarly, we obtain the *square of the lever over radius of gyration ratio* being $\left(\frac{\mu_i}{r_{iy}}\right)^2 = \left(\frac{6.4}{33.4}\right)^2 = 0.037$ for the pitch motion and 1.0 for the surge motion. The surge and pitch motions contribute 96.4% and 3.6% to total energy absorption respectively. The pitch motion contribution is quite limited. The resulting strain energy dissipation is 56.7 MJ versus 58.9 MJ from USFOS simulation, which is reasonably accurate.

6. Conclusions

This paper presents numerical modelling and dynamic response analysis of a 10 MW semi-submersible floating offshore wind turbine subjected to ship collision loads. The striking ships include a modern supply vessel of 7500 tons and a shuttle tanker of 150,000 tons. Wind turbines in both parked and operative conditions are considered. The following conclusions are drawn:

1. The studied semi-submersible floating wind turbine is in general safe when it is subjected to collisions from modern supply vessels with a design energy of 37 MJ for bow collisions and 21 MJ for side collisions. The nacelle accelerations, however, exceed the allowable operational limit and may damage the delicate equipment inside the nacelle. For shuttle tanker collision with a kinetic energy of 420 MJ, the FOWT will undergo large displacements and rotations and may eventually lose hydrostatic stability and capsize.
2. It is generally more critical when ship collision occurs on an operating floating wind turbine, and the worst case is when the vessel strikes from the opposite of the wind direction. Wind thrust loads on turbine blades will induce a negative pitch angle of the platform. During collision, the combined actions of collision loads, wind thrust and the tightened mooring lines may significantly amplify the pitch motion and cause possible

Table 12
Proof and breaking loads of the mooring chain according to DNV OS E302 [28].

Material grade	Grade R3 with a yield stress 410 MPa		Grade R5 with a yield stress 760 MPa	
chain diameter [mm]	proof load [MN]	breaking load [MN]	proof load [MN]	breaking load [MN]
137	9.67	13.82	13.82	19.84

Table 13
Strain energy dissipation from USFOS analysis and external dynamic calculations.

Case number	state of the FOWT	total initial kinetic energy [MJ]	strain energy from USFOS [MJ]	strain energy by the analytical model [MJ]	Deviation [%]
column1-180deg- supply vessel bow	parked	37	27.0	29.7	10.0
column1-90deg- supply vessel bow	parked	37	21.0	22.4	6.7
column1-180deg- supply vessel side	parked	21	13.9	15.9	14.4
column1-90deg- supply vessel side	parked	21	10.4	11.5	10.6
column1-180deg-tanker side	parked	420	58.9	56.7	−3.7
column2-0deg-tanker side	parked	420	30.5	27.8	−8.9
column1-180deg- supply vessel bow	operative	37	27.2	29.7	9.2
column2-0deg- supply vessel bow	operative	37	22.3	23.9	7.2
column1-180deg- supply vessel side	operative	21	14.2	15.9	12.0
column2-0deg- supply vessel side	operative	21	11.5	12.3	7.0

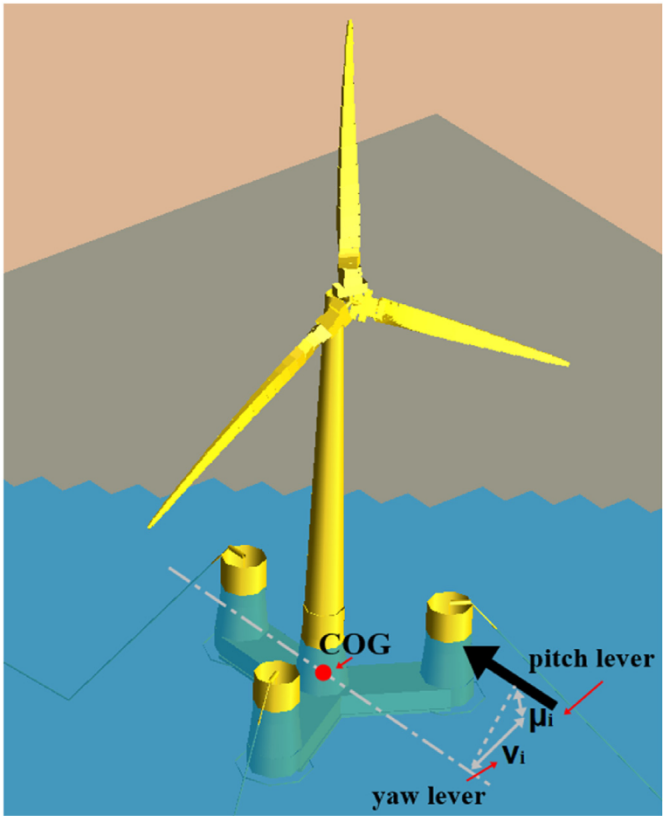

Fig. 39. Illustration of using the simple formulas to predict energy dissipation for the case column2-0deg-tanker side.

capsizing of the floater. In addition, the wind loads also increase tower bending moments and nacelle accelerations, and therefore increase the risk of tower buckling and exceedance of the nacelle operational limits.

3. The compliance of a floating offshore wind is favorable with respect to ship collisions. Floating wind turbines are therefore capable of resisting impacts of much higher energy without collapse compared to bottom fixed installations.
4. The simple external dynamic model is capable of predicting the dissipated strain energy in the ship-FOWT collisions with quite good accuracy up to the point of maximum force during first and generally most violent impact (repetitive impacts may take place). The influence of tower flexibilities on the structural damage to the floater is limited for the studied FOWT.

Credit author

Zhaolong Yu: Conceptualization, Modelling, Simulation, Validation, Writing – review & editing. Jørgen Amdahl: Conceptualization, Methodology, Supervision, Writing – review & editing, Project administration, Funding acquisition. Martin Rypestøl: Modelling, Simulation, Validation, Writing. Zhengshun Cheng: Calculation of aerodynamic loads in HAWC2

Declaration of competing interest

The authors declare that they have no known competing financial interests or personal relationships that could have appeared to influence the work reported in this paper.

Acknowledgement

The authors gratefully acknowledge the financial support by Research Council of Norway via the Centers of Excellence funding scheme, project number 223254 – NTNU AMOS. The authors would also like to thank the support from high performance computation resources from the Norwegian national e-infrastructures, Project NN9585K - Accidental actions on strait crossings and offshore platforms.

Appendix A. Supplementary data

Supplementary data to this article can be found online at https://doi.org/10.1016/j.renene.2021.12.002.

References

[1] L. Ramírez, D. Fraile, G. Brindley, Offshore Wind in Europe: Key Trends and Statistics 2019, 2020.
[2] G. DNV, DNV GL-ST-0119 Floating Wind Turbine Structures, DNV GL, Høvik, Norway, 2018.
[3] F. Biehl, E. Lehmann, Collisions of Ships with Offshore Wind Turbines: Calculation and Risk Evaluation, Offshore Wind Energy: Springer, 2006, pp. 281–304.
[4] A. Bela, H. Le Sourne, L. Buldgen, P. Rigo, Ship collision analysis on offshore wind turbine monopile foundations, Mar. Struct. 51 (2017) 220–241.
[5] P.T. Pedersen, Ship Collisions against Wind Turbines, Quays and Bridge Piers. Collision and Grounding of Ships and Offshore Structures—Proceedings of the 6th International Conference on Collision and Grounding of Ships and Offshore Structures, ICCGS, 2013, pp. 273–281.
[6] R. Kroondijk, High Energy Ship Collisions with Bottom Supported Offshore Wind Turbines, Institutt for marin teknikk, 2012.
[7] H. Le Sourne, A. Barrera, J.B. Maliakel, Numerical crashworthiness analysis of an offshore wind turbine jacket impacted by a ship, J. Mar. Sci. Technol. 23 (2015) 694–704.
[8] T. Pire, H. Le Sourne, S. Echeverry, P. Rigo, Analytical formulations to assess the energy dissipated at the base of an offshore wind turbine jacket impacted by a ship, Mar. Struct. 59 (2018) 192–218.
[9] M. Song, Z. Jiang, W. Yuan, Numerical and Analytical Analysis of a Monopile-Supported Offshore Wind Turbine under Ship Impacts, Renewable Energy, 2020.
[10] S. Echeverry, L. Márquez, P. Rigo, H. Le Sourne, Numerical crashworthiness analysis of a spar floating offshore wind turbine impacted by a ship. Developments in the Collision and Grounding of Ships and Offshore Structures, in: Proceedings of the 8th International Conference on Collision and Grounding of Ships and Offshore Structures (ICCGS 2019), 21-23 October, 2019, CRC Press, Lisbon, Portugal, 2019, p. 85.
[11] A. Pegalajar-Jurado, F. Madsen, M. Borg, H. Bredmose, Qualification of Innovative Floating Substructures for 10MW Wind Turbines and Water Depths Greater than 50m, LIFES50+ project report, 2015.
[12] Dr techn, Olav olsen AS, URL, http://www.olavolsen.no/.
[13] C. Bak, F. Zahle, R. Bitsche, T. Kim, A. Yde, L.C. Henriksen, et al., The DTU 10-MW Reference Wind Turbine, Danish Wind Power Research 2013, 2013.
[14] T. Soreide, J. Amdahl, E. Eberg, O. Hellan, T. Halmås, USFOS—a computer program for progressive collapse analysis of steel offshore structures. Theory Manual SINTEF Report STF71 F, 1999, p. 88038.
[15] Z. Yu, J. Amdahl, A review of structural responses and design of offshore tubular structures subjected to ship impacts, Ocean Eng. 154 (2018) 177–203.
[16] Y. Sha, J. Amdahl, C. Dørum, Local and global responses of a floating bridge under ship–girder collisions, J. Offshore Mech. Arctic Eng. 141 (2019), 031601.
[17] Z. Yu, J. Amdahl, D. Kristiansen, P.T. Bore, Numerical analysis of local and global responses of an offshore fish farm subjected to ship impacts, Ocean Eng. 194 (2019) 106653.
[18] C. Bak, F. Zahle, R. Bitsche, T. Kim, A. Yde, L.C. Henriksen, et al., Description of the DTU 10 MW reference wind turbine, DTU Wind Energy Report-I-0092 5 (2013).
[19] A. Pegalajar-Jurado, F. Madsen, M. Borg, H. Bredmose, State-of-the-art models for the two LIFES 50+ 10MW floater concepts. tech. rep, 2018.
[20] I. Wamit, Wamit User Manual, Chestnut Hill, USA, 2006.
[21] T.J. Larsen, A.M. Hansen, How 2 HAWC2, the User's Manual. December 2007, 2007.
[22] N-003, N. NORSOK N-003: 2016: Actions and Actions Effects, Norsok Lysaker, Norway, 2016.
[23] DNV-RP-C204, Recommended Practice DNV-RP-C204, DET NORSKE VERITAS, 2016.
[24] R. Tørnqvist, Design of Crashworthy Ship Structures, Technical University of Denmark Kgns Lyngby, Denmark, 2003.
[25] DNV-RP-C204, Recommended Practice DNV-RP-C204, DET NORSKE VERITAS, 2019.
[26] H. Kjeøy, J. Amdahl, Impacts and Collisions Offshore Progress Report No. 8 Ship Impact Forces in Collision with Platform Legs, DNV report, 1979.
[27] D.N. Veritas, Buckling Strength of Shells, Recommended Practice DNV-RP-C202, Det Nor Ver Class AS, Veritasveien, 2010, p. 1.
[28] DNVGL, DNVGL OS E302, Offshore Mooring Chains, 2015.
[29] Y.N. Popov, O. Faddeev, D. Kheisin, A. Yakovlev, Strength of Ships Sailing in Ice, U.S. Army Foreign Science and Technology Center (Translation), 1967.